THE ASTROPHYSICAL JOURNAL, 435:416–434, 1994 November 1

EVIDENCE FOR A DISK IN THE WIND OF HD 93521: UV LINE PROFILES FROM AN AXISYMMETRIC MODEL[1]

J. E. BJORKMAN, R. IGNACE, T. M. TRIPP, AND J. P. CASSINELLI
Department of Astronomy, University of Wisconsin, 475 North Charter Street, Madison, WI 53706
Received 1994 February 25; accepted 1994 May 6

ABSTRACT

Recently it has been suggested (Massa 1992; Howarth & Reid 1993), from the C IV ultraviolet resonance line profile of HD 93521, that there is a high-speed component in the polar outflow from the star as well as a low-speed component in the equatorial regions. In this paper we present theoretical calculations of the line profiles that would be produced by such a model. We find from *Hubble Space Telescope* Goddard High Resolution Spectrograph observations of HD 93521 that the observed C IV profile can be produced if the star has an inclination angle very close to 90° and if the star is surrounded by a thin disk, whose half-width is approximately 3° in latitude. The geometry of this disk is similar to what one would expect from the wind-compressed disk model of Bjorkman & Cassinelli, so this star may provide an ideal observational test of that model.

In addition to the C IV resonance line, we examine both the Si IV and N V resonance lines. The Si IV line exhibits low-velocity absorption that is similar to that seen in the C IV line, but the emission is much weaker. The absorption component is well fitted by the geometry that is inferred from the C IV line. It appears that the weaker emission from the polar component arises because Si IV is one stage below the dominant state, Si V. On the other hand, the N V line has weaker absorption and much stronger emission than the C IV line. N V is a higher ionization state than C IV, so it is likely that N V is one stage above the dominant state, N IV. The correlation of the emission strength of these three ions with their ionization state suggests that there are latitudinal ionization gradients that occur because the density increases from the pole to the equator.

Apart from fitting individual line profiles, we also examine the differences between the two *Hubble Space Telescope* observations of HD 93521. We find evidence for a pair of narrow absorption components, seen at low velocity, as well as evidence for a discrete *emission* feature in the blueshifted absorption cores of the lines. This blueshifted emission at low velocity can cause what instead appears to be an interstellar absorption line. Without multiple observations that can reveal the temporary emission, one must be very careful when determining interstellar column densities to stars like HD 93521.

Subject headings: stars: individual (HD 93521) — stars: mass loss — ultraviolet: stars

1. INTRODUCTION

HD 93521 is a bright, $m_v = 7.04$ (Guetter 1974), early-type, O9.5 V (Hobbs et al. 1982) star at a high Galactic latitude ($l = 183°$, $b = 62°$). Its location makes it extremely useful as a probe of the interstellar medium (e.g., Spitzer & Fitzpatrick 1992). However, the object's position has resulted in considerable controversy over its origin and age. It has a small radial velocity, $v_r = -14$ km s^{-1} (Howarth & Reid 1993), and if it formed in the Galactic disk, its large height, $z = 1.5$ kpc, above the Galactic plane implies an age that is larger than its main-sequence lifetime (Irvine 1989).

To address this paradox, there have been suggestions that HD 93521 is instead an evolved Population II object. An evolved star would have a larger radius, lower luminosity, and smaller distance. Based on the Hγ equivalent width and Hα photometry, Bisiacchi et al. (1978) determine that HD 93521 has a luminosity class of Ib–II. However, as pointed out by Irvine (1989), who found evidence for Hα emission, HD 93521 may be a shell star, so any spectral classification based on the strength of the hydrogen lines is potentially inaccurate.

A different approach for obtaining the stellar radius was employed by Ramella, Morossi, & Santin (1980), as well as Ebbets & Savage (1982). They used stellar wind theory to estimate the stellar escape speed, v_{esc}, from measurements of the wind terminal speed, v_∞, because the escape speed indirectly determines the stellar radius. Assuming $v_\infty = 3v_{esc}$ (the average for several O stars found by Abbott 1978), they found that HD 93521 is a low-mass evolved Population II object. However, Irvine (1989) notes that the more recent terminal speed measurements of Prinja & Howarth (1986) indicate that, for the late spectral type of O 9.5, $v_\infty = 1.3v_{esc}$. With this value for the escape speed, Irvine finds that HD 93521 would be a main-sequence star. Additional support for this conclusion is provided by Howarth & Reid (1993), who find that the escape speed of the evolved Population II solutions would imply that the star rotates faster than its break-up speed, v_{crit}. Consequently, it now appears that HD 93521 is a Population I star, and the paradox of how it has attained such a large height above the Galactic plane remains.

In addition to the location, a number of spectroscopic characteristics of HD 93521 are very unusual. It exhibits narrow absorption components (NACs) at displacement velocities much smaller than is normally seen (Prinja & Howarth 1986). Conti & Ebbets (1977) found that the star has a $v \sin i$ of 400 km s^{-1}, which is one of the largest measured. It has a UV

[1] Based on observations made with the NASA/ESA *Hubble Space Telescope*, obtained at the Space Telescope Science Institute, which is operated by the Association of Universities for Research in Astronomy, Inc., under NASA contract NAS5-26555.

continuum deficit, as shown by Massa (1992) who analyzed both *IUE* and *HST* spectra. This in conjunction with the large $v \sin i$ suggests that the star may directly exhibit the effects of gravity darkening. Most recently, Howarth & Reid (1993) and Fullerton (1994) studied the nonradial pulsation (NRP) characteristics of this star and found that the star is a nonradial pulsator ($l = -m \approx 9$) with a period of 1.8 hr.

Our particular interest in this star is the suggestion that there may be an equatorial disk in the stellar wind. This geometry was proposed by Massa (1992) and Howarth & Reid (1993) because the stellar spectrum shows a plateau or shelflike feature connecting a high-velocity absorption edge to a low-velocity absorption edge in the C IV ($\lambda\lambda$1548, 1551 Å) P Cygni profile (see Fig. 2). One component is a high-speed wind in the polar regions, and the second component is a low-speed "disk" in the equatorial regions. Note, however, that the "shelf" is not present in the Si IV and N V profiles. There is additional evidence of a disk due to similarities to Be stars, which are also thought to be surrounded by dense equatorial disks. First, as previously mentioned, HD 93521 may be a shell star (Irvine 1989; Massa 1992). Second, there is evidence for double-peaked Hα emission with a central self-reversal (Irvine 1989; Howarth & Reid 1993; Fullerton 1994). Finally, there is the presence of nonradial pulsations (Howarth & Reid 1993; Fullerton 1994). Since HD 93521 is a rapid rotator, there is also a theoretical reason to suppose that it may have an equatorial wind-compressed disk (Bjorkman & Cassinelli 1993).

The main purpose of this paper will be to investigate how a two-component wind geometry affects the UV resonance line profiles, and what can be determined about the geometry of the disk. Specifically, using the SEI method (Sobolev plus Exact Integration) of Lamers, Cerruti-Sola, & Perinotto (1987) with modifications for an axisymmetric geometry (Bjorkman, Sembach, & Watson 1994), we have been able to produce line profiles that exhibit shelflike structures at large velocity. Furthermore, these shelf-features appear only if the star is close to edge-on and if the disk is quite thin.

The organization of this paper is as follows: We present the spectra of HD 93521 from the *Hubble Space Telescope* and discuss their implications in § 2. In § 3 we review the SEI methodology and introduce the modifications for an axisymmetric wind. The effects of a two-component geometry on the UV resonance line profiles are described in § 4. Finally, in § 5 we apply our model to the specific case of HD 93521.

2. GHRS OBSERVATIONS OF HD 93521

HD 93521 was observed on 1991 January 4 and June 15 with the *Hubble Space Telescope* (*HST*) Goddard High Resolution Spectrograph (GHRS) as part of the instrument's in-flight science verification program (Ebbets 1992).

2.1. *Observations and Data Reduction*

The observations were obtained with a variety of intermediate- and low-resolution gratings, instrument set-ups, and apertures. As a result, the spectral coverage is quite good. Using the large science aperture (LSA), the star was observed with the G140M, G160M, G200M, G270M, and G140L gratings, and additional small science aperture (SSA) observations were carried out with the G160M, G200M, and G270M gratings (see Table 2 in Savage 1991 for a brief summary of GHRS grating properties; see also Ebbets 1992). The intermediate-resolution LSA observations provided spectral coverage from $\sim$1150 to $\sim$1950 Å, but the SSA observations only covered 1232–1269 Å, 1307–1343 Å, 1382–1418 Å, 1532–1568 Å, 1793–1828 Å and 1834–1874 Å. Additional intermediate resolution observations were obtained over limited wavelength ranges longward of 2000 Å.

The resolution of observations made with the SSA is not severely affected by the well-publicized spherical aberration of the *HST* that was present prior to 1993 December. Although the *HST* point-spread function had a complex 4″ halo (see Burrows et al. 1991), the SSA only passed the well-focused core into the instrument. Consequently, the intermediate resolution gratings provided resolutions of $\sim$12–15 km s^{-1} with the SSA.

Although the spherical aberration did not seriously affect the SSA resolution, the core of the point-spread function contained only $\sim$15% of the light from a point source, so SSA observations suffered a serious reduction of throughput compared to the prelaunch specifications. One could recover much of the throughput by using the LSA, but the resolution was degraded and the spectroscopic spread function had a sharp core with broad wings. For further discussion of the effects of the spherical aberration on GHRS spectrsocopy, we refer the reader to Savage (1991), Gilliland et al. (1992), Spitzer & Fitzpatrick (1993), Sofia, Savage, & Cardelli (1993), and Gilliland & Hulbert (1993).

In this paper we primarily use the LSA data because the signal-to-noise (S/N) is significantly better than the SSA data. Some of the HD 93521 spectra were obtained with substep pattern 4, which provides 2 samples per diode to satisfy the Nyquist sampling requirement. Other observations were obtained with substep pattern 5, which provides 4 samples per diode. Unfortunately, for these science verification observations, the FP-SPLIT procedure was not used, and consequently the spectra contain fixed pattern noise due to irregularities on the detector faceplate and photocathode (the FP-SPLIT procedure reduces fixed pattern noise by using four different grating positions that shift the spectrum, in each exposure, by $\sim$5 diodes on the detector; when these subexposures are coadded in wavelength space, the fixed pattern noise is partially averaged out). However, for most of the purposes of this paper, the signal-to-noise obtained without the FP-SPLIT procedure is certainly adequate. Note that the S/N of the individual GHRS spectra are significantly better than the S/N of *International Ultraviolet Explorer* (*IUE*) high-dispersion observations of HD 93521.

A log of the GHRS observations employed in this paper is given in Table 1. The table lists the *HST* archive identification number, universal time when the observation was begun, exposure duration, samples per diode, aperture, and spectral range of each observation. The exposure durations listed in Table 1 are on-target durations; with two samples per diode, an additional 12.5% of the on-target exposure duration was used for background observations; with four samples per diode, an additional 6.25% of the on-target exposure duration was devoted to background observations. For this project we have elected to use only the observations made with the G160M grating because (1) this is the only grating that was used on January 4 *and* June 15 (we wanted to compare observations made with the same grating), (2) the G140M spectra contain more bad diodes and fixed pattern noise (but are otherwise of comparable quality), and (3) we are primarily interested in the P Cygni lines shortward of 2000 Å.

The data were reduced with the CALHRS software at the GHRS computing facility at the Goddard Space Flight Center (CALHRS is also part of the standard Space Telescope Science

TABLE 1

GHRS INTERMEDIATE-RESOLUTION OBSERVATIONS OF HD 93521[a]

HST Archive ID Number	UT Exposure Start (Year, Day, Hour:Min:Sec)	Exposure Duration[b] (s)	Samples (diode^{-1})	Aperture[c]	Spectral Range (Å)
Z0EQ0115T	1991,004,14:09:01.6	50.7	2	LSA	1206.7–1242.8
Z0EQ0116T	1991,004,14:10:37.6	50.7	2	LSA	1238.9–1274.9
Z0EQ0117T	1991,004,14:12:04.6	50.7	2	LSA	1270.9–1306.9
Z0EQ0118T	1991,004,14:13:45.6	50.7	2	LSA	1302.0–1337.9
Z0EQ0119T	1991,004,14:15:26.6	50.7	2	LSA	1333.8–1369.6
Z0EQ011AT	1991,004,14:17:01.6	50.7	2	LSA	1367.0–1402.7
Z0EQ011BT	1991,004,14:18:37.6	50.7	2	LSA	1398.8–1434.4
Z0EQ011CT	1991,004,14:20:13.6	50.7	2	LSA	1430.7–1466.2
Z0EQ011DT	1991,004,14:21:49.6	50.7	2	LSA	1462.6–1498.1
Z0EQ011ET	1991,004,14:23:36.6	50.7	2	LSA	1495.6–1530.9
Z0EQ011FT	1991,004,14:25;17.6	50.7	2	LSA	1526.6–1561.9
Z0EQ011GT	1991,004,14:26:51.6	50.7	2	LSA	1557.9–1593.0
Z0EQ011HT	1991,004,14:28:25.6	50.7	2	LSA	1590.6–1625.5
Z0EQ011IT	1991,004,14:29:52:6	50.7	2	LSA	1623.4–1658.3
Z0EQ011JT	1991,004,14:31:33.6	50.7	2	LSA	1655.6–1690.4
Z0EQ011KT	1991,004,14:33:14.6	50.7	2	LSA	1686.3–1720.9
Z0EQ011LT	1991,004,14:34:41.6	50.7	2	LSA	1718.4–1752.9
Z0EQ011MT	1991,004,14:36:22.6	50.7	2	LSA	1750.5–1784.9
Z0EQ011NT	1991,004,14:38:03.6	50.7	2	LSA	1784.0–1818.2
Z0EQ011OT	1991,004,14:39:37.6	50.7	2	LSA	1815.6–1849.7
Z0EQ011PT	1991,004,14:41:04.6	50.7	2	LSA	1847.2–1881.2
Z0EQ011QT	1991,004,14:42:45.6	50.7	2	LSA	1880.0–1913.8
Z0EQ011RT	1991,004,14:44:26.6	50.7	2	LSA	1911.0–1944.7
Z0EQ011ST	1991,004,14:46:01.6	50.7	2	LSA	1943.4–1977.0
Z0K6520FT	1991,166,12:10:53.5	25.3	4	LSA	1232–1269
Z0K6520PM	1991,166,13:46:59.5	25.3	4	LSA	1307–1343
Z0K6520ZM	1991,166,15:24:05.5	50.7	4	LSA	1307–1343
Z0K65219M	1991,166,17:03:29.5	50.7	4	LSA	1532–1568
Z0K6521JM	1991,166,18:42:53.5	50.7	4	LSA	1793–1828
Z0K6520IT	1991,166,12:19:19.5	38.0	4	SSA	1232–1269
Z0K6520SM	1991,166,13:55:20.5	38.0	4	SSA	1307–1343
Z0K65212M	1991,166,15:34:07.5	76.0	4	SSA	1382–1418
Z0K6521CM	1991,166,18:03:07.5	76.0	4	SSA	1532–1568
Z0K6521MM	1991,166,19:45:25.5	76.0	4	SSA	1793–1828

[a] All observations listed in this table were carried out with the G160M grating. Additional observations of HD 93521 with the G140M, G200M, G270M, and G140L gratings were obtained as part of the GHRS Science Verification program, and Spitzer & Fitzpatrick 1992, 1993 have observed this star with the GHRS echelle mode.

[b] On-target exposure duration. An additional 6.25% or 12.5% of the on-target exposure duration was used for background observations.

[c] LSA ≡ large science aperture, and SSA ≡ small science aperture.

Institute pipeline and IRAF reduction packages). The data reduction includes conversion to count rates, correcting for particle radiation, diode nonuniformities, dark counts, paired pulse events (where applicable), background subtraction, and wavelength calibration using the standard calibration tables available at the Space Telescope Science Institute. Note that the default wavelength calibration tables have been shown to be as accurate as wavelength calibrations based on WAVECAL/SPYBAL exposures (Lindler 1993). The full HD 93521 spectrum observed with the GHRS on 1991 January 4, and reduced as described above is shown in Figure 1*a*.

One problem with the calibration of the data is that the sensitivity of the GHRS at a given wavelength depends on the spatial location of the spectrum on the detector (Ebbets 1992); toward the edge of the detector, the sensitivity is lower than at the center. This effect is referred to as "vignetting" in the final report of the GHRS Science Verification Program, but this term is mildly misleading, because only a fraction of the vignetting is caused by obscuration in the optical path. This decrease in sensitivity toward the detector edge is also due to gradients in the photocathode quantum efficiency, blemishes and scratches on the detector faceplate, and to loss of light off the edge of the detector. Since GHRS vignetting depends on the spatial location of the spectrum on the detector, and since the spectrum location on the detector is variable from one observation to the next, it is very difficult to incorporate an exact vignetting correction into the data reduction software, and in some cases the CALHRS vignetting functions do not adequately correct for vignetting, which causes edge effects at the 5%–20% level. Unfortunately, as we will see later, this vignetting affects some of the data in the P Cygni line profiles of HD 93521.

2.2. *Continuum Placement*

Continuum placement is a critical issue when comparing theoretical P Cygni profiles to observations, because the relative amount of emission and absorption in the profile is sensitive to the inferred continuum location. To continuum-normalize the spectra, we fitted a fifth-order Legendre polynomial to the continuum longward of 1300 Å; shortward of 1300 Å, we used a second-order Legendre polynomial. These fits are shown by dashed lines in Figure 1*a*. Due to the large $v \sin i$ of HD 93521, the photospheric absorption lines are often blended, and continuum placement is consequently somewhat

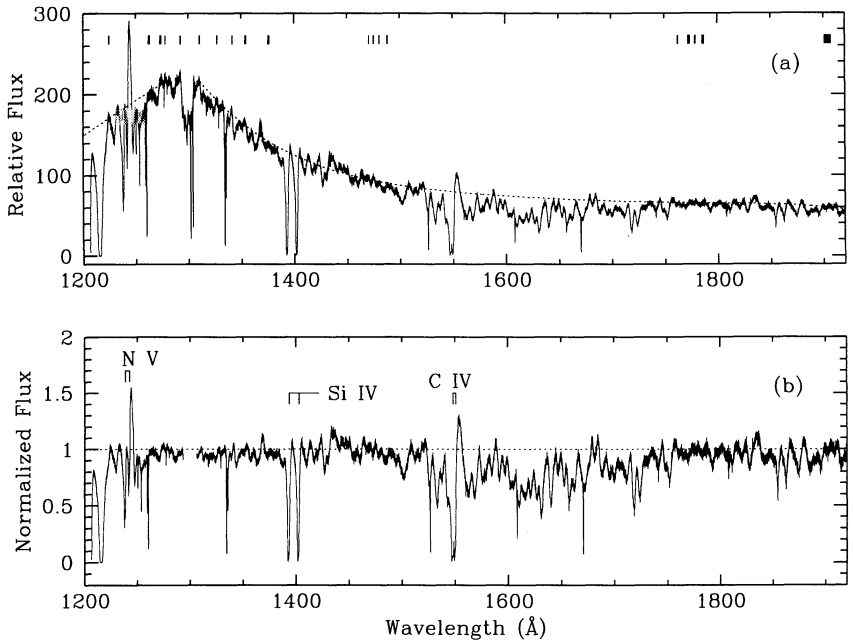

FIG. 1.—Ultraviolet spectrum of HD 93521 (O 9.5 V, $m_v = 7.04$). The spectrum was obtained with the *Hubble Space Telescope* Goddard High Resolution Spectrograph (GHRS) on 1991 January 4. Shown in the top panel (*a*) is the relative flux (counts s^{-1} $diode^{-1}$) vs. wavelength (Å) in the heliocentric reference frame. The dashed lines show our polynomial fits to the continuum; the regions to which the polynomials were fit are indicated by bars near the top of the panel. The bottom panel (*b*) shows the normalized spectrum, which is produced by dividing the data shown in panel (*a*) by the continuum fit. The locations of the N V, Si IV, and C IV doublets are indicated.

difficult; we tried to select line-free regions by locating sections of the spectrum that are "relatively flat" over a range of several Å. The regions of the spectrum that were used for the polynomial fits are indicated by bars near the top of Figure 1*a*. The normalized spectrum is shown in Figure 1*b*, and is obtained by dividing the GHRS data by the continuum fits.

From the normalized spectrum, we extracted individual line profiles for Si IV, C IV, and N V. The profiles obtained on both 1991 January 4 and June 15 are plotted in Figure 2 (note that both sets of spectra were normalized with the same continuum, shown in Fig. 1*a*). Recently Howarth & Reid (1993) discussed *IUE* observations of the Si IV, C IV, and N V profiles of HD 93521. Although Howarth & Reid's Si IV and N V continuum placements are similar to ours, the continuum placement they used to normalize their C IV profile is significantly different from the C IV continuum we adopted (compare Howarth & Reid's Fig. 3 to our Fig. 2). The continuum placement employed by Howarth & Reid (1993) results in a C IV wind profile that contains strong absorption out to an edge at ~ -500 km s^{-1}, weaker absorption extending to a second edge at ~ -1200 km s^{-1}, and *emission at high negative velocities* extending from the second edge out to ~ -2000 km s^{-1}. High-velocity wind emission blueward of the absorption is very peculiar. Howarth & Reid (1993) note that the emission is "a unique circumstance in our experience of the UV spectra of normal O stars." On the other hand, the C IV profile that is obtained using our continuum level does not show any high-velocity emission blueward of the P Cygni absorption (see Fig. 2).

Which C IV continuum placement is correct? This question is difficult to answer definitively due to line blanketing and the high rotation rate of the star. Howarth & Reid (1993) compare the C IV P Cygni profile to its mirror image (see their Fig. 4). They observe that the mirror image of the redshifted emission matches the blue part of the profile between -1500 km s^{-1} (the second absorption edge) and -2000 km s^{-1}. Because wind emission is symmetric about zero velocity, and since the shape of the blue part of the profile agrees with its mirror image, they argue that there is blueshifted wind emission at higher velocities than the wind absorption. Thus, they claim that the polar terminal velocity, v_∞^p, must be at least 2000 km s^{-1}.

If there are absorption lines on either side of the C IV wind line, there might be a problem with Howarth & Reid's argument, because, if the absorption lines are of similar equivalent widths and have the correct wavelengths, they could mimic the effect observed by Howarth & Reid. Perhaps it is improbable that there would be lines on both sides of C IV with the correct wavelengths and strengths, but, for example, there could be Fe III line blanketing on *both* sides of the C IV line, as discussed by Kurucz (1974) and Swings & Vrieux (1976). As seen in Figure 2 of Swings & Vrieux, the strongest Fe III lines are at 1532 Å (-3100 km s^{-1}), 1539–1540 Å (-1900 to -1500 km s^{-1}), 1546–1547 Å (-500 to -100 km s^{-1}), 1550–1552 Å (300 to 800 km s^{-1}), and 1556 Å (1600 km s^{-1}). There are also numberous weak Fe III lines across the entire range. Regardless of whether or not Fe III is present in HD 93521, a *Copernicis* spectrum (Rogerson & Upson 1977) of a somewhat cooler low $v \sin i$ star, τ Sco (B0 V), shows numerous lines in the regions of 1530.2–1534.0 Å (-3500 to -2700 km s^{-1}), 1536.6–1539.5 Å (-2200 to -1700 km s^{-1}), and 1555.6–1557.4 Å (1400 to 1800 km s^{-1}). The spectrum of τ Sco ends at 1560 Å, so we do not know whether there are additional lines longward of 1560 Å. Noting that the rapid rotation of HD 93521 will broaden these lines, examination of the C IV profile shown in Figure 2 reveals that the two absorption features shortward of -1500 km s^{-1} may be due to the same lines that are observed in τ Sco. In support of this conclusion, a rotationally broadened spectrum of the low $v \sin i$ star μ Col (O 9.5 V) also shows the same two absorption features shortward of -1500 km s^{-1} (D. Massa,

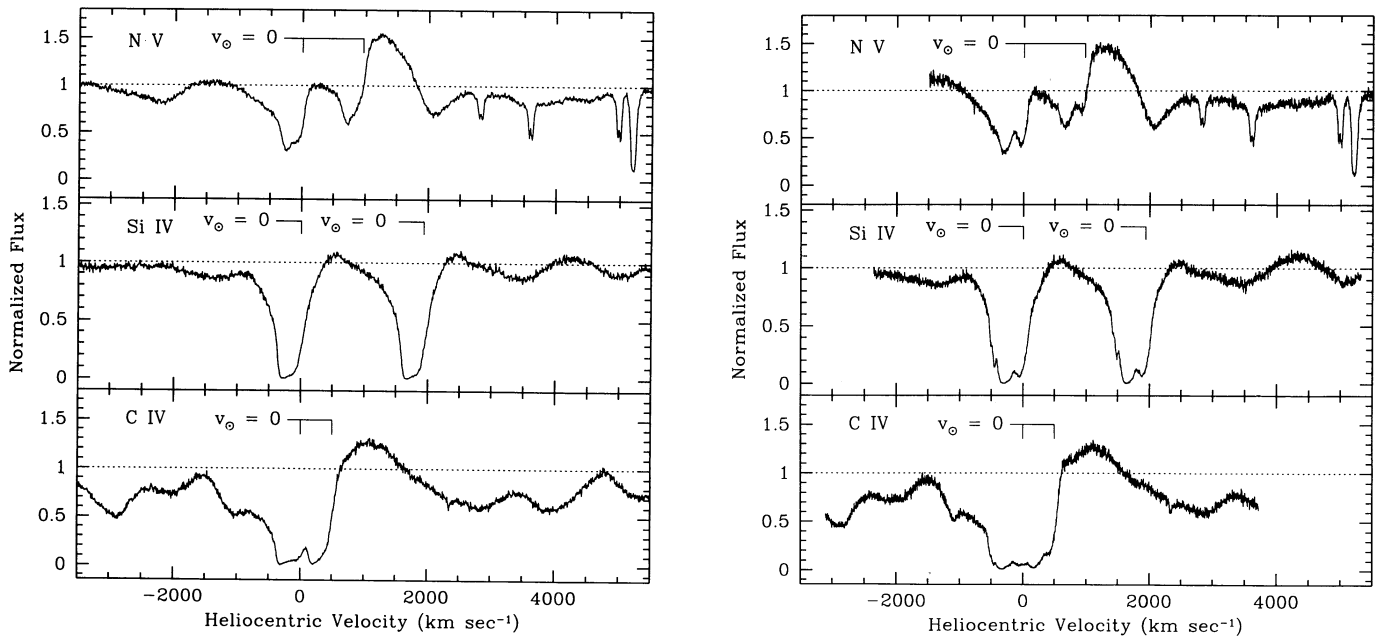

FIG. 2.—Normalized N v, Si IV, and C IV line profiles. The left panel shows the data obtained 1991 January 4, and the right panel shows the 1991 June 15 data. The June 15 data were normalized using the same continuum as the January 4 data. Both observations were made with the GHRS using the large science aperture (LSA). The normalized flux is plotted versus heliocentric velocity in the velocity frames of N v 1239 Å, Si IV 1394 Å, and C IV 1548 Å; $v_\odot$ indicates the heliocentric zero velocity of each line in the doublet. Note the plateau or shelflike feature in the C IV absorption profile that extends from the low-velocity edge at roughly -400 km s^{-1} to the bottom of the high-velocity edge at roughly -1200 km s^{-1}. Examination of a spectrum of low v sin i star μ Col (O 9.5 V) reveals that the small absorption feature at the blue end (-1000 km s^{-1}) of the "shelf" is probably of photospheric origin.

1994 private communication). Thus there may not be any emission blueward of -1500 km s^{-1}. There is also no evidence of any blueshifted emission in either our or Howarth & Reid's N v profiles.

Our continuum is based on a low-order polynomial fit to line-free regions over a broad (600 Å) range of the stellar continuum, so it is less likely to be affected by the metal line blanketing. On the other hand, since C IV is formed outside the photosphere, it can be argued that if the stellar photosphere is line blanketed (Kurucz 1974 found that for a rapidly rotating B2 star, the maximum emergent intensity near C IV is 83% of the continuum), then the effective continuum for the C IV line is the average (over the C IV line width) of the emergent intensity of the stellar atmosphere. It is therefore very difficult to determine the value of the effective continuum.

2.3. *Profile Variability and NACs*

In this section we examine the P Cygni profile variability and narrow absorption components (NACs) revealed by the GHRS observations. In Figure 3 we plot the normalized GHRS HD 93521 spectra obtained on 1991 January 4, on top of the normalized spectra obtained on 1991 June 15. Figure 3 shows abundant P Cygni profile variability at low and intermediate velocities but does not show clear variability above the noise shortward of ~ -1500 km s^{-1}. The small differences between January 4 and June 15 at the short wavelength edges of the N v and C IV spectra and the long-wavelength edge of the Si IV spectrum are due to the GHRS vignetting previously discussed. Interesting features in Figure 3 include (1) an apparent increase in the edge-velocity of the low-velocity absorption component, (2) changes in the structure of the line core at low velocities (<200 km s^{-1}), and (3) variability at the right edge of the C IV and Si IV absorption that *extends through zero velocity* (i.e., to small redshifts).

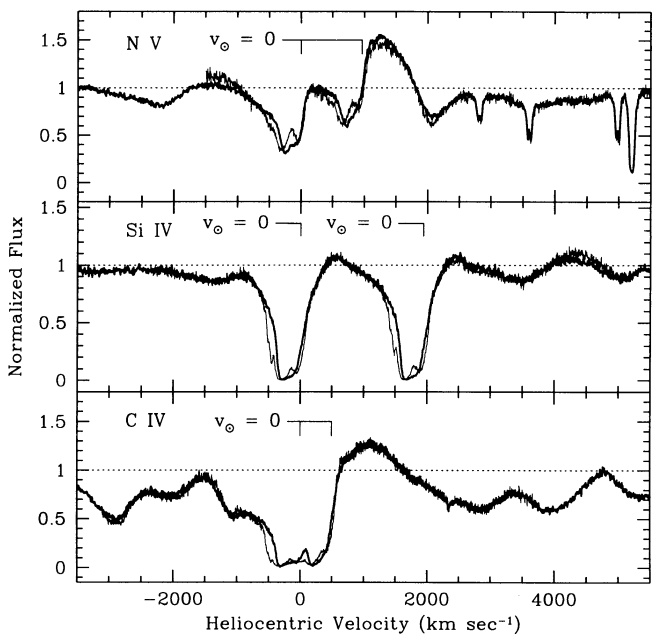

FIG. 3.—Comparison of the June 15 line profiles (*thin line*) to the January 4 line profiles (*thick line*). To account for flux calibration errors, the June 15 profiles were scaled to match the January 4 data in spectral regions that are not affected by the stellar wind. The discrepancies between the January 4 and June 15 data near spectrum cutoffs (e.g., the difference between the N v profiles at -1500 km s^{-1} and the difference between the Si IV profiles at $\sim +4300$ km s^{-1}) are due to instrumental vignetting. Variability can be seen from the high-velocity edge of C IV (-1500 km s^{-1}) to above zero velocity in the Si IV profile. Most noticeable is the blue edge variability of the low-velocity component (-400 to -500 km s^{-1}) as well as an apparent emission bump at about -150 km s^{-1} in all three line profiles.

One might worry that the variability redward of zero velocity might be either noise or instrumental errors. However, as seen from the smoothness of the curve over several pixels, the change is larger than the random noise. Assuming the same continuum shape for both *HST* observations, the redshifted variability is also larger than the uncertainty owing to the measurement errors in our continuum normalization factor. Finally, the change is the same for *both* components of the Si IV doublet; this argues that the variability is not due to wavelength-dependent sensitivity variations of the instrument. We conclude, therefore, that the redshifted variability is probably significant and not of instrumental origin.

In Figure 4 we compare the January 4 GHRS wind profiles to the average of 10 high-dispersion *IUE* spectra of HD 93521 obtained in 1987 March over a period of 7 hours (these are the 12 spectra used by Howarth & Reid 1993 minus two spectra that were not available at the NDADSA archive). This comparison shows clear variability up to ~ -1500 km s^{-1} in all three lines. We have also compared these data to the average of two large aperture high-dispersion *IUE* spectra obtained in 1988 March (SWP33180 and SWP33181); these failed to show any variability shortward of -1500 km s^{-1}. Based on the observed variabiity we conclude that the edge-velocity is the same for all three lines and is about -1500 km s^{-1}.

To examine the low velocity variability and profile structure in greater detail, we present expanded plots of the P Cygni profiles between -800 and $+200$ km s^{-1} in Figure 5. Inspection of the January 4 and June 15 profiles, compared in Figures 3 and 5, reveals the following: (1) between 0 and -500 km s^{-1}, variability is clearly detected, and the variability is at least partially due to changing discrete absorption *and emission* with the absorption component of the line; (2) multiple NACs are present in the Si IV profiles obtained on June 15; these are probably also present in the C IV profiles and possibly the N V profile; (3) no obvious NACs or discrete emission components are apparent in the January 4 profiles redward of -800 km s^{-1}; and (4) the low-velocity edge at ~ -500 km s^{-1} appears to have shifted by roughly -100 km s^{-1} between 1991 January 4 and June 15.

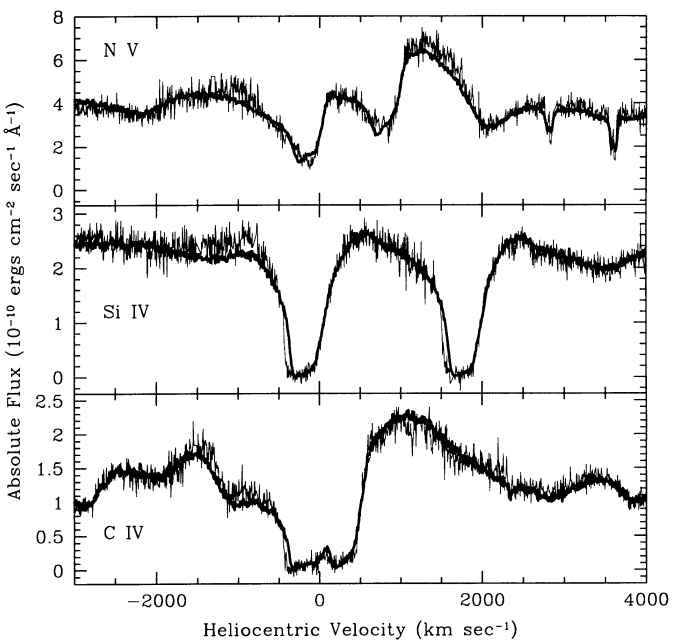

FIG. 4.—Comparison of the *HST* UV line profiles obtained with the GHRS on 1991 January 4 (*thick line*) to the average of 10 *IUE* spectra obtained over a 7 hour period in March of 1987 (*thin line*). Again to account for calibration errors, the GHRS data have been scaled slightly to lie on top of the *IUE* data in regions well removed from the wind profiles. The variability seen in this comparison agrees with that seen in Fig. 3: there is variability detected up to ~ -1500 km s^{-1}, and the low-velocity blue edge in the *IUE* data is shifted by ~ -100 km s^{-1} compared to the GHRS data.

The apparent shift of the low-velocity edge may be entirely due to the June 15 NACs, however. In Figure 6 we show the SSA Si IV spectrum obtained on 1991 June 15, and with the improved resolution of the SSA, two sharp and strong NACs are readily seen at -464 and -532 km s^{-1}. These NACs are not as obvious in the SSA C IV and N V profiles, but the SSA data are noisy. The LSA C IV and N V data have better S/N and do show excess absorption at the velocities of the Si IV NACs (see Fig. 5), so the NACs are probably present, though unresolved, in these profiles. We conclude, therefore, that the apparent shift of the edge-velocity is not due to a change in the terminal speed of the low-velocity component, but is instead an artifact of the NACs, which must be present in the high-velocity component.

The most unusual feature of the low-velocity variability is the appearance of excess emission, compared to the January 4 data, at about -150 km s^{-1} in *all* of the June 15 profiles (see Fig. 5). This emission bump could be an intrinsic part of the P Cygni profiles that is absorbed in the January 4 data by low-velocity NACs or the broad low-velocity absorption enhancements that Prinja (1988) and Prinja & Howarth (1988) have suggested are the precursors of NACs. However, the smoothness of the January 4 profiles argues against this interpretation, especially in the unsaturated N V profiles; it is unlikely that NACs or NAC precursors would have just the right width and depth to perfectly remove the excess emission observed on June 15, leaving the smooth profiles of January 4. Consequently, we believe that the June 15 emission excess is discrete emission in the wind. It is interesting that the emission blob appears when the somewhat higher velocity NACs appear and is not present when the NACs are not present. We do not know of any previous detections of low-velocity emission blobs in the wind profiles of stars of this spectral type.

The January 4 C IV profile also shows a bump at low velocity, but this bump does not occur at the same velocity in the red (1548 Å) and blue (1551 Å) components. It is also not present in the Si IV and N V profiles. We will see in § 5.1.1. that this bump is not due to a density enhancement in the wind, but it is probably instead a line blending effect arising from the juxtaposition of the strong low-velocity absorption of the red and blue components of C IV. Note that this bump does not appear in the June 15 data. However, the NACs of the red component are at the velocity where the January 4 bump would have occurred, so it has probably been hidden by the NACs.

As an aside, we note that the low-velocity variability of the Si IV, C IV, and N V P Cygni profiles poses a serious problem for studies of the highly ionized interstellar medium in the direction of HD 93521. If one were to interpret the 1991 June 15 profiles alone, one might conclude that there is strong interstellar absorption by all three of these species extending from 0 to -150 km s^{-1} (see Fig. 5). *However, there is no evidence of interstellar absorption in the January 4 P Cygni profiles.* Therefore, very little of what appears to be interstellar absorption is truly due to interstellar gas (if it were, it would be unchanging and would have a detectable effect on the January 4 data).

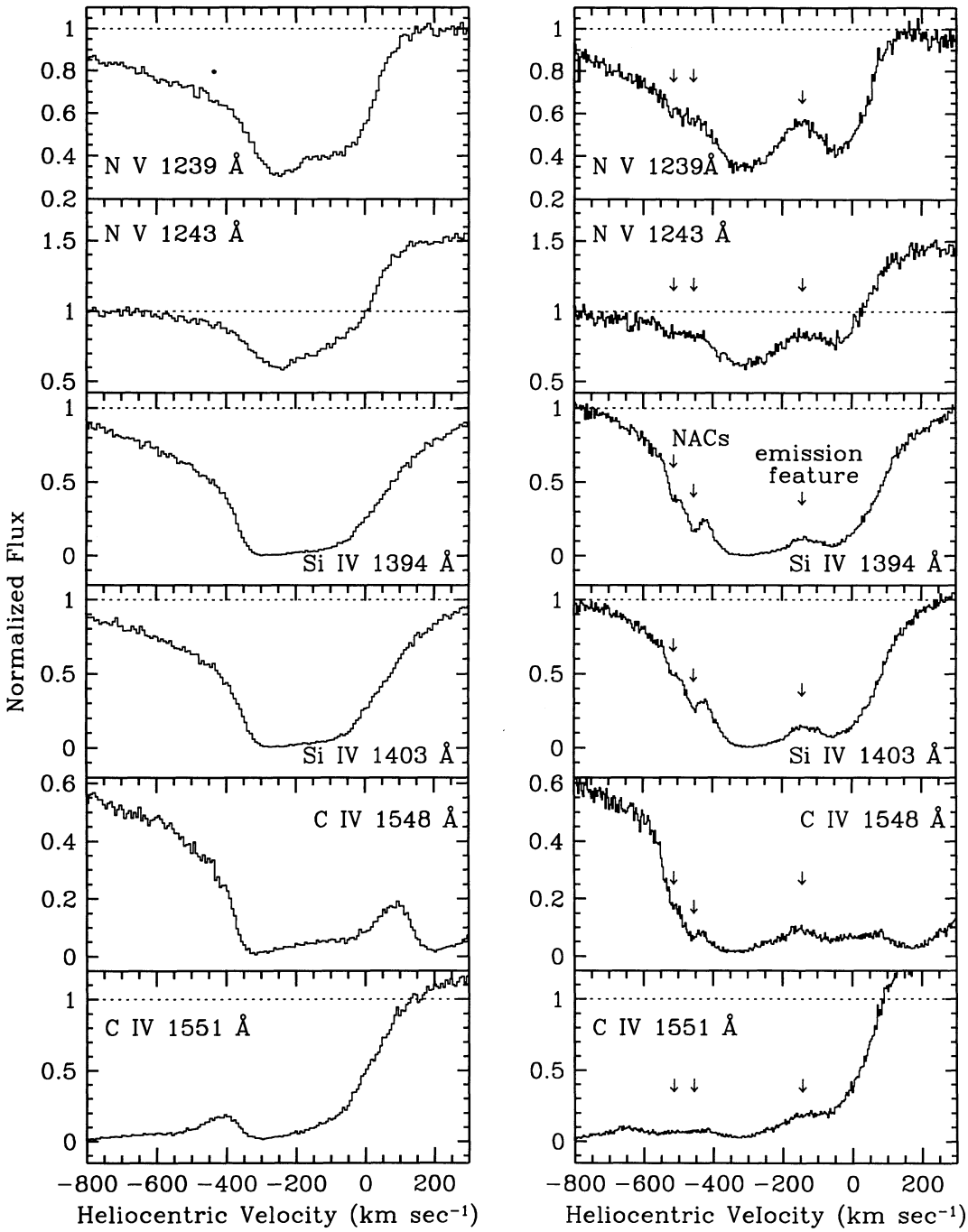

FIG. 5.—Expanded plots of the normalized line profiles recorded by the GHRS on 1991 January 4 (*left panel*) and 1991 June 15 (*right panel*) using the LSA. There are striking differences between the January 4 profiles and the June 15 profiles in this velocity range. NACs are detected in the June 15 Si IV profiles at -464 and -532 km s^{-1} (see the higher resolution SSA profile shown in Fig. 6). The positions of the Si IV NACs are marked with arrows in the right panel. These NACs are probably also detected in the C IV 1548 Å profile and possibly in the N V profiles. The June 15 profiles also show excess emission at ~ -150 km s^{-1} when compared to the January 4 profiles (the position of this emission feature is also indicated with an arrow in the right panel). Note that the emission feature appears to be strongest in the N V profile. These features seen in the June 15 profiles are not readily apparent in the January 4 profiles.

Instead, the apparent absorption is probably due to structure in the wind, as suggested above. Even if there is a significant interstellar component in the P Cygni profiles, it is probably very difficult to disentangle from the stellar components.

Spitzer & Fitzpatrick (1992) have obtained GHRS echelle observations of HD 93521 to study highly ionized interstellar halo gas in this direction. Spitzer & Fitzpatrick are appropriately cautious about their GHRS data and state that "the complexity of the underlying stellar spectrum (arising from the presence of stellar wind features) makes it difficult to determine the precise depth of the interstellar features or whether there is more widespread interstellar absorption in their general regions." Because of their concerns about stellar contamination of the interstellar profiles, Spitzer & Fitzpatrick limit their analysis to the narrow components of the Si IV and C IV profiles observed between -50 and -100 km s^{-1}. The data

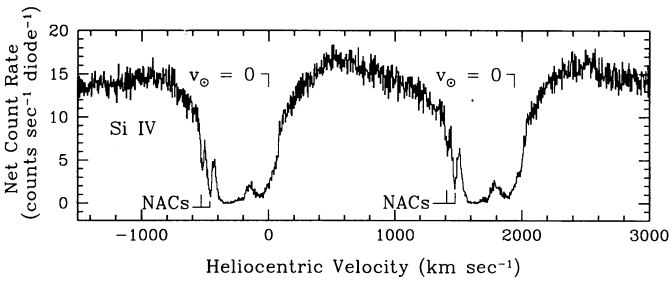

FIG. 6.—Observations of the HD 93521 Si IV line profiles obtained with the GHRS on 1991 June 15 using the small science aperture (SSA). The positions of NACs and the heliocentric zero velocity for both lines are shown. Since the resolution of SSA observations is not degraded by the *HST* spherical aberration, the NACs are much more readily apparent in this spectrum. Qualitatively, these NACs appear to be unusually sharp and strong.

shown in Figure 5 confirm Spitzer & Fitzpatrick's concerns: the broader part of the Si IV and C IV profiles shown in their Figure 2 is clearly of stellar origin. The narrow Si IV and C IV absorption between -50 and -100 km s^{-1} that Spitzer & Fitzpatrick attribute to the ISM is not apparent in our data, but we might not have sufficient resolution and S/N to detect this feature.

3. THE MODEL

Integral to the study of hot luminous stars is the determination of mass-loss rates and wind structure by using models to fit the profiles of ultraviolet P Cygni lines. Castor (1970) employed the Sobolev approximation in his calculation of line profiles in Wolf-Rayet stars. He assumed a spherically symmetric wind, and the source function was determined using the statistical equilibrium of a two-level atom after accounting for the penetration and escape probabilities of photons under the Sobolev approximation. More detailed calculations have been made using the co-moving frame method (Mihalas, Kunasz, & Hummer 1975; Hamann 1980, 1981). Hamann (1981) noted that the source function calculated using the Sobolev method agreed quite well with the source function calculated with the co-moving frame method, so most of the discrepancies between the two methods lay in the solution to the transfer equation. With this idea in mind, Lamers et al. (1987) developed the SEI method (Sobolev with Exact Integration). In the SEI method, the source function is calculated using the Sobolev approximation, and the formal solution to the transfer equation is directly integrated using a realistic (i.e., finite Doppler width) line profile function.

The above methods have all employed spherically symmetric geometries, so they must be modified for an axisymmetric geometry, such as a disk model. A generalization of the Sobolev method for arbitrary geometries and velocity laws is presented by Rybicki & Hummer (1978). Using Rybicki & Hummer's generalized Sobolev method, Mazzali, Berger, & Henrichs (1990) investigated the effects of rotation on P Cygni line profiles. Mazzali et al. (1990) integrated the transfer equation using the Sobolev approximation, so their work is an extension of Castor's (1970) one-dimensional spherically symmetric model to two-dimensional axisymmetric geometries. Similarly, Bjorkman, Sembach, & Watson (1994) have extended the one-dimensional spherically symmetric SEI method to a two-dimensional axisymmetric geometry. In their method the source function is again calculated using the Sobolev approximation, and the transfer equation is integrated directly using a line profile function with a finite Doppler width.

Unlike a spherically symmetric wind that has a monotonically increasing velocity, an axisymmetric rotating wind may have nonlocal coupling of the source functions between different parts of the atmosphere. Neither Mazzali et al.'s nor Bjorkman et al.'s methods account for nonlocal coupling of line photons. This is a reasonable approximation if the stellar contribution to the mean intensity dominates any contribution from other parts of the envelope. This may be true for singlet lines; however, for doublets it is well known that the blue component can contribute a significant fraction of the photons to the red component (Olson 1982). For this reason, both methods are currently limited to singlet line profiles.

This study of the wind of HD 93521 will employ the two-dimensional SEI method of Bjorkman et al. (1994) using a two-component wind model. A complete description of the computational aspects of the model will not be given here. Rather, we will concentrate on the physics of the model and a qualitative description of the method in the next section. We refer the reader to Lamers et al. (1987) for a complete description of the SEI method and to Bjorkman et al. (1994) for a description of its two-dimensional extension.

3.1. *The SEI Method*

As previously mentioned, the SEI method uses the Sobolev approximation for calculating the source function. The intensity is computed by a numerical integration of the transfer equation instead of an analytical solution resulting from the Sobolev formalism. The optical depth, τ_ν, intensity, I_ν, and flux, F_ν, are respectively given by

$$\tau_\nu = \int_z^\infty \kappa \phi_\nu \, dz \,, \tag{1}$$

$$I_\nu = \begin{cases} \int_{z_*}^{\infty} \kappa \phi_\nu S_\nu e^{-\tau_\nu} dz + e^{-\tau_\nu} I_\nu^* & (p < R_*) \,, \\ \int_{-\infty}^{+\infty} \kappa \phi_\nu S_\nu e^{-\tau_\nu} dz & (p > R_*) \,, \end{cases} \tag{2}$$

$$F_\nu = \int_0^{2\pi} d\alpha \int_0^\infty I_\nu(p, \alpha) p \, dp \,, \tag{3}$$

where R_* is the stellar radius, $z_* = (R_*^2 - p^2)^{1/2}$ is the z-coordinate of the stellar surface, I_ν^* is the stellar intensity, κ is the line opacity, and ϕ_ν is the line profile function. Note that the line profile function, which we assume is Gaussian, must contain the Doppler shifts that account for the expansion of the envelope (see eqs. [1] and [8] of Rybicki & Hummer 1978). The line of sight coordinates (z, p, α) that are used for the integrations are illustrated in Figure 7. The source function, S_ν is

$$S_\nu = \frac{\beta_c I_\nu^* + \epsilon B_\nu}{\beta + \epsilon} \,, \tag{4}$$

where β_c and β are the penetration and escape probabilities as defined by equations (103) and (34) in Rybicki & Hummer (1978), ϵ is the ratio of collisional to radiative de-excitations, and B_ν is the Planck function in the wind.

For an O 9.5 V star, such as HD 93521, the mass-loss rates are low enough that we may assume that collisional (de)excitations are negligible. This implies that ϵ is zero, so the source function reduces to

$$S_\nu = \frac{\beta_c}{\beta} I_\nu^* \,. \tag{5}$$

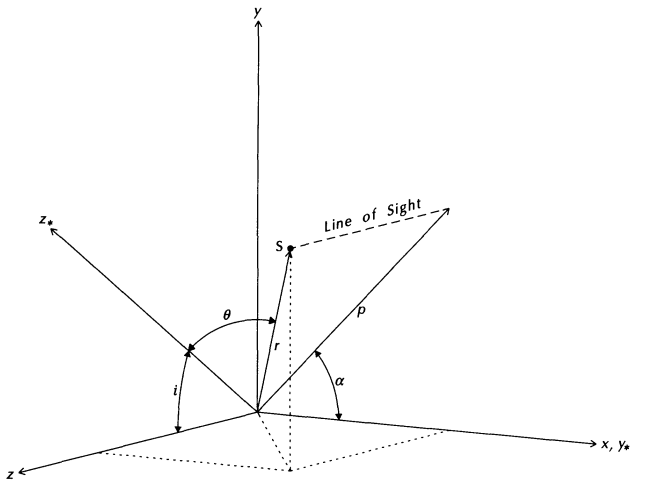

FIG. 7.—Coordinate system used for integrating the flux from the star, which is at the origin. The observer is at $+\infty$ on the z-axis. The line of sight passing through the point, S, has a position angle, α, and impact parameter, p, on the plane of the sky, the x-y plane. The stellar rotation axis, z_*, is inclined by an angle, i, and the point, S, has spherical polar coordinates (r, θ) in the stellar reference frame.

To use the equations above to calculate line profiles, we must specify the velocity and opacity as a function of position.

3.2. *Two-Component Winds*

This section outlines the parameterization of the stellar envelope, which is used by our routine for calculating the line profiles. To incorporate an axisymmetric geometry, the following changes are made to the one-dimensional SEI method: both the density and outflow velocities now become functions of the radius, r, and polar angle, θ (see Fig. 7). The velocity,

$$\boldsymbol{v} = v_r(r, \theta)\hat{r} + v_\theta(r, \theta)\hat{\theta} + v_\phi(r, \theta)\hat{\phi} , \tag{6}$$

has three components. For the r-component of the velocity, we assume a standard "β-law." In general the θ-component of the velocity will be nonzero (see Bjorkman & Cassinelli 1993); however, for simplicity, we assume that $v_\theta = 0$ so that the streamlines lie on surfaces of constant θ. Note that in the case, the streamlines spiral out along the surface of a cone. Finally, in an axisymmetric geometry, there are no torques about the z-axis, so angular momentum conservation determines the ϕ-component of the velocity. These velocity components are

$$v_r = v_0 + (v_\infty - v_0)\left(1 - \frac{R_*}{r}\right)^\beta , \tag{7}$$

$$v_\theta = 0 , \tag{8}$$

$$v_\phi = V_{\rm rot} \sin\theta \left(\frac{R_*}{r}\right) , \tag{9}$$

where $V_{\rm rot}$ is the stellar rotation speed, v_0 is the initial velocity (we assume $v_0 = 0.01 v_\infty$), and β controls how quickly v_r approaches its asymptotic value of v_∞. For simplicity we use $\beta = 1$ (radiatively driven stellar winds typically have $\beta \approx 0.8$). The terminal speed, v_∞, is a function of latitude and is assumed to be of the form

$$v_\infty(\theta) = v_\infty^p + (v_\infty^{\rm eq} - v_\infty^p) f(\theta) , \tag{10}$$

where $f(\theta)$ ranges between 0 and 1 and controls the transition from one component to the next. We have chosen

$$f(\theta) = \frac{1}{2}\left[1 + \frac{2}{\pi}\arctan\left(\frac{\mu_d - \mu}{\Delta\mu_d}\right)\right] , \tag{11}$$

which approximates a step function. We have used the usual definition that $\mu = \cos\theta$ and $\mu_d = \sin(\Delta\theta_d)$, where $\Delta\theta_d$ is the half-width of the disk in latitude. Note that our choice for $f(\theta)$ employs an analytic instead of a discontinuous function; this is motivated by the requirement that adaptive mesh numerical integrators have analytic integrands. The parameter, $\Delta\mu_d$, controls the width in latitude (i.e., the thickness) of the transition region from the polar terminal speed, v_∞^p, to the equatorial (i.e., disk) terminal speed, $v_\infty^{\rm eq}$. Typically we employ a very small $\Delta\mu_d$ of 0.001 (so that $\Delta\mu_d \ll \mu_d$). Note that at the midpoint of the transition region, v_∞ is equal to the mean, $(v_\infty^p + v_\infty^{\rm eq})/2$.

For the θ-dependent mass-loss rate, we assume a similar form:

$$\dot{M}(\theta) = \dot{M}_p + (\dot{M}_{\rm eq} - \dot{M}_p) f(\theta) . \tag{12}$$

This mass-loss rate is the mass flux at the stellar surface multiplied by $4\pi R_*^2$. To obtain the density from the mass-loss rate, we use the continuity equation. Since the streamlines diverge with constant solid angle, mass conservation implies that

$$\rho = \frac{\dot{M}(\theta)}{4\pi r^2 v_r(r, \theta)} . \tag{13}$$

It is also useful to define a dimensionless density, $\bar{\rho} \equiv \rho/\rho_0$, where

$$\rho_0 = \frac{\dot{M}_p}{4\pi R_*^2 v_\infty^p} . \tag{14}$$

Now that we have specified the flow geometry, we next must determine the opacity to be used for calculating line profiles. Using the two usual two-level atom approximation, we have that

$$\kappa = \frac{\pi e^2}{m_e c} gf\left(\frac{n_1}{g_1} - \frac{n_2}{g_2}\right) , \tag{15}$$

where f is the oscillator strength, n_1 and n_2 are the number densities of atoms in the lower and upper levels, respectively, and g is the multiplicity of the level. Because of the NLTE conditions typical in an extended atmosphere, most atoms are in the ground state. So, for a resonance line, we expect that $n_1 \gg n_2$, and that

$$n_1 = q_i A_E n_{\rm H} = q_i A_E X \frac{\rho}{m_{\rm H}} , \tag{16}$$

where X is the mass fraction of hydrogen, A_E is the elemental abundance (by number) relative to hydrogen, and q_i is the fraction of the element in the ith ionization stage.

If we assume that the ionization rates are dominated by photoionization and radiative recombination, then the ionization fraction is proportional to $(W/\rho)^{\Delta i}$, where the dilution factor, $W = 0.5(1 - [1 - (R_*/r)^2]^{1/2})$, and Δi is the difference between the ion stage, i, and the dominant stage (e.g., if one were fitting the C IV line when C II is the dominant state, then $\Delta i = 2$). This scaling law produces an ionization fraction that asymptotically approaches a constant at large radii; the resulting line profile tends to have the maximum absorption at

high velocity, which produces a sharp blueshifted absorption edge at the terminal velocity of the wind. However, many lines (usually weak ones) do not have a sharp edge, but instead the maximum absorption occurs at low velocity with a gradual return back to the continuum level at the terminal speed of the wind. Lamers & Morton (1976) fitted such lines using a Sobolev optical depth that is proportional to $(1 - v/v_\infty)^\gamma$; having adopted $\beta = 1$, this is equivalent to assuming that the ionization fraction $q_i \propto (R_*/r)^\alpha$, where $\alpha = \gamma$ (Lamers et al. 1987). Following Lamers et al. (1987), we combine these two factors and adopt the following scaling law for the ionization fraction:

$$q_i = \frac{q_{1/2,i}}{q_{0,i}} \left(\frac{W}{\bar{\rho}}\right)^{\Delta i} \left(\frac{R_*}{r}\right)^{\alpha} . \tag{17}$$

The normalization constant, $q_{0,i}$, is chosen so that $q_{1/2,i}$ is the ionization fraction where $v/v_\infty = 1/2$ and $\theta = 0$. For $\beta = 1$, this occurs at $r/R \approx 2$, so

$$q_{0,i} \approx \left(\frac{1}{2}\right)^{\alpha} \left(1 - \frac{\sqrt{3}}{2}\right)^{\Delta i} . \tag{18}$$

We have specified the physical ingredients required for calculating line profiles. Next, there is the practical question of what is the minimum set of parameters necessary to uniquely specify a model. First are the parameters required to specify the geometry and flow velocities. These include the rotation velocity, $V_{\rm rot}$, the polar terminal speed, v_∞^p, the terminal speed ratio, $v_1 = v_\infty^{\rm eq}/v_\infty^p$, the disk opening angle, $\Delta\theta_d$, and the stellar inclination angle, i. Second are the parameters that control the ionization balance; these are the abundance, A_E, ionization fraction, $q_{1/2}$, line state, Δi, and the radial exponent, α. Finally, to obtain the density, we must specify the polar mass-loss rate, $\dot{M}_p$ and the ratio, $\dot{M}_0 = \dot{M}_{\rm eq}/\dot{M}_p$.

Initially it would appear that all of these parameters are required to uniquely specify a model. However, once we have specified the geometry and velocities, the line profile depends only on the opacity, κ, as a function of position. Since $\kappa \propto n_i$, the profile depends on the product of the mass-loss rate, $\dot{M}_p$, ionization fraction, $q_{1/2,i}$, and elemental abundance A_E. Rather than independently specifying these parameters, we only need to specify one constant that determines the opacity (i.e., their product). Following Castor & Lamers (1979) we choose the integrated *polar* optical depth defined by

$$T = \int_0^1 \tau(w) dw = \int_{R_*}^{\infty} \frac{\kappa c}{v_0 v_\infty^p} \bigg|_{\theta=0} dr , \tag{19}$$

where $\tau = (\kappa c/v_0)\,|dv/dr|^{-1}$ is the Sobolev optical depth in the radial direction, and $w = v_r/v_\infty^p$. One advantage of using this definition is that the total optical depth, T, directly determines the column density, N_i, of the ion. As shown by Lamers et al. (1987),

$$N_i = \left(\frac{m_e c}{\pi e^2}\right)\left(\frac{v_\infty^p}{f_{12}\lambda_0}\right) T . \tag{20}$$

We may use this column density to find the polar mass-loss rate. The column density is defined as $N_i = \int n_i dr$, where n_i is the number density for a given ion species, i. Substituting the number density, equation (16), and employing equations (13) and (17) to eliminate the density and ionization fraction, we find that

$$N = \left(\frac{\dot{M}_p}{4\pi R_* v_\infty^p m_{\rm H}}\right) X A_E q_{1/2,i} \frac{I(\Delta i, \alpha)}{q_{0,i}} , \tag{21}$$

where

$$I(\Delta i, \alpha) = \int_{R_*}^{\infty} \left(\frac{W}{\bar{\rho}}\right)^{\Delta i} \left(\frac{R}{r}\right)^{\alpha} \bar{\rho} \frac{dr}{R_*} . \tag{22}$$

Solving for the mass-loss rate gives

$$\dot{M}_p q_{1/2,i} = 4\pi R_* v_\infty^p \left(\frac{m_{\rm H} N_i}{X A_E}\right) \frac{q_{0,i}}{I(\Delta i, \alpha)} . \tag{23}$$

We can compare the column densities of two different lines. Calculating the ratio of the previous equation with that for a second line (denoted by primes), and solving for the ratio of ionization fractions gives

$$\frac{q_{1/2,i} A_E}{q_{1/2,i'} A'_E} = \frac{q_{0,i} I(\Delta i', \alpha')}{q_{0,i'} I(\Delta i, \alpha)} \left(\frac{N_i}{N_{i'}}\right) . \tag{24}$$

From the two preceding equations, we see that the column density can be used in several ways: First, it can be used to estimate the mass-loss rate, *if* one knows the abundance and ionization fraction. Second, by examining the ratio of the column densities for lines of two different elements, one can determine information on the relative abundances in the wind, *if* one knowns the relative ionization fractions. Finally, the ratio of column densities for two different ionization stages of the same element can be used to estimate the relative ionization fractions of the two different stages. The column densities and mass-loss rates derived from our fits to HD 93521 are presented and discussed in § 5.2. Before proceeding to our fits of HD 93521, we first present general results on the line profiles that can be produced by a two-component geometry.

4. RESULTS FROM THE TWO-COMPONENT MODEL

This section is divided into two parts. The first discusses how a two-component geometry leads to the formation of a profile with two absorption-edges. The second is a parameter study that explores the range in line profiles that one may obtain in this model.

4.1. *Two-Component Line Profiles*

To qualitatively understand the shape of a line produced by a two-component geometry, we first consider the absorption and emission independently produced by each of the two components for an optically thick line. For the edge-on observer, shown in Figure 8, the absorption and emission for each component is schematically shown in Figure 9.

The absorption for the polar component (Fig. 9*a*) has the usual P Cygni shape *except* at high velocities. This is because, for a given line of sight velocity, v_z, the disk produces a "hole" in the corresponding iso-velocity surface of the polar component; it no longer covers the entire solid angle of the star, so the observed flux is larger. In going from small to large velocities, the iso-velocity surfaces are farther from the star, the hole is bigger, and the observed flux increases. This produces the upward slope in the absorption out to the edge-velocity instead of the usual flat bottom with a sharp blue edge. Note that the high-velocity edge is not determined by the polar terminal speed but rather by the radius, r_c, at which the disk covers the entire star (see Fig. 8). Thus, $v_{\rm edge}^p = v_r^p(r_c)$. The loca-

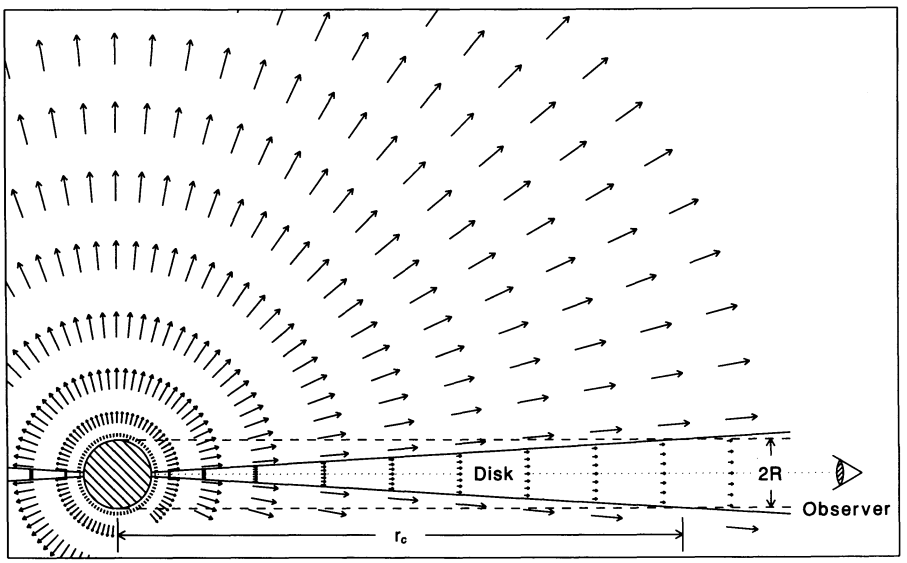

FIG. 8.—Meridional cross section that shows the geometry of the two-component wind. The star (hatched region in the lower left corner) is oriented so that its rotation axis is in the vertical direction, so the disk is shown edge-on. The arrows are the velocity vectors of the wind. Note that the velocity in the disk component is one-sixth the velocity in the polar component. For the observer (shown at right), the fluid contained in the cylindrical column in front of the star (region between the dashed lines) is responsible for producing the absorption part of the line profile. Note that the disk covers the entire solid angle of the star only at radii larger than the covering radius, r_c. Similarly, the polar component almost completely covers the star at small radii (i.e., small velocity), but at large radii (i.e., large velocity) it covers very little, if any, of the star.

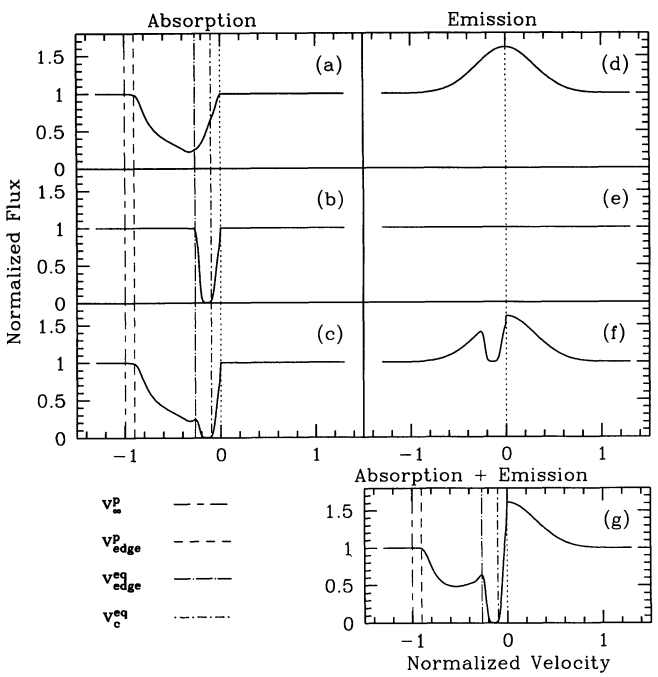

FIG. 9.—Line formation in a two-component wind. The wind geometry used is similar to that used for the fit to the HD 93521 C IV line. Each panel shows a plot of normalized flux (F_v/F^*_v) vs. normalized velocity (v/v^p_∞). At left, panels (*a–c*) show the absorption of the stellar flux by the wind; at right, panels (*d–f*) show the emission produced by the wind. Top to bottom: the flux produced by the polar component (*a* and *d*); flux produced by the disk component (*b* and *e*); and the flux produced by the combination of both components (*c* and *f*). Finally, panel *g* shows net result of combining the wind absorption with the wind emission. The legend at the bottom left refers to the vertical lines used to mark special velocities discussed in the text.

tion of the maximum absorption depth of the profile depends on the details of the model. This is because the depth depends on both the size of the hole and on the Sobolev optical depth through the iso-velocity surface. The Sobolev optical depth is proportional to $\kappa |dv/dr|^{-1}$. At small radii, the velocity gradient is large, and the line is optically thin. So as $v_z \rightarrow 0$, the absorption depth decreases to zero.

The disk-component absorbs out to the terminal speed of the disk, v^{eq}_∞, and produces a sharp absorption-edge at $v^{eq}_{edge} = v^{eq}_\infty$ (see Fig. 9*b*). Going blueward from zero velocity, the solid angle covered by the disk increases until at the velocity, $v^{eq}_c = v^{eq}_r(r_c)$, the entire stellar disk is finally covered. The lack of covering explains why the disk absorption is not black at low velocities. Finally, note that for a given line of sight velocity, v_z, the disk-component is closer to the observer than the polar component (see Fig. 8). The polar component is therefore seen behind the disk component, and the net absorption profile (Fig. 9*c*) is approximately the product of the two individual absorption profiles.

The emission produced by the polar and disk-components is shown in Figures 9*d* and 9*e* respectively. Even though the disk emission appears flat, there is in fact emission at about the 1% level. The disk component has little emission, compared to the polar region, because of its small projected area when viewed edge-on. Since the polar emission is observed through the disk, the total emission is approximately given by the polar emission times the disk absorption plus the disk emission; the net emission is shown in Figure 9*f*.

Finally, the total combined profile is obtained by summing the net emission and absorption profiles. The combined profile is shown in Figure 9*g*. This profile illustrates the typical shape of a two-component wind viewed edge-on—a P Cygni profile from the polar component plus a low-velocity absorption component from the disk.

4.2. *Parameter Study*

In this section, we explore the parameter space of the two-component wind model. There are six fundamental parameters that describe the envelope geometry: (1) the mass-loss rate in the disk (relative to the polar mass-loss rate), $\dot{M}_0$, (2) the total optical depth, T, (3) the line-of-sight inclination of the system, i, (4) the terminal speed of the disk (relative to the polar terminal speed), v_1, (5) the disk opening angle, $\Delta\theta_d$, and (6) the ionization stage (relative to the dominant ionization stage), Δi, which controls the ionization balance in the wind. As our base model, we chose parameters that fit the C IV profile of HD 93521 (the parameters are given in Tables 3 and 4). In each of the following six figures (Figs. 10–15), we change one parameter while keeping the others fixed, as indicated in the figure legends.

Figure 10 shows how the low-velocity absorption component increases as the mass-loss rate in the disk is increased until the low-velocity profile becomes completely saturated. Note that for $\dot{M}_0 = 0.1$, the optical depth in the disk is still greater than that in the pole because of the small terminal speed in the disk. Interestingly, there is not the corresponding increase in the emission at low velocities that one would expect in a spherically symmetric model (for which the absorption and emission equivalent widths are equal). Although for a scattering line the total number of photons is conserved, in an axisymmetric geometry these photons no longer escape isotropically.

Figure 11 shows how the profile changes as a function of total optical depth, T. Both the high-velocity absorption and emission increase with polar optical depth, and the absorption equivalent width (ignoring the disk component) is approximately equal to the emission equivalent width. This is because the polar component is almost spherically symmetric. The disk component is largely unaffected because the large mass-loss ratio, $\dot{M}_{eq}/\dot{M}_p$, implies that the disk absorption is almost saturated even at the smallest polar optical depth.

Figure 12 shows the effects of inclination angle, i, on the line profile. Note that the disk absorption is only seen for angles which place the observer within the opening angle of the disk (i.e., $i > 90° - \Delta\theta_d$). This is because the disk must cover the entire solid angle of the star with optically thick material to produce a black profile. As the inclination angle is decreased from edge-on ($i = 90°$), only the highest velocities in the disk cover the entire solid angle, so the lowest velocity absorption begins to decrease. As the inclination angle passes $i \approx 90° - \Delta\theta_d$, the high velocity material covers half of the stellar disk, so the disk absorption is at most 50% black. Consequently, the entire low-velocity absorption component disappears. Finally, when viewing the system pole-on ($i = 0°$), the disk produces a relatively narrow emission spike at low velocity. This is because the large optical depth in the disk produces significant emission, and the projected area is largest for the polar direction. Furthermore, the line of sight velocity spread, $v_\infty^{eq} \sin \Delta\theta_d$, is quite small since the disk is so thin.

Figure 13 shows the effect of changing the terminal speed in the disk. As expected, the low-velocity absorption-edge moves to higher velocity as the terminal speed of the disk is increased;

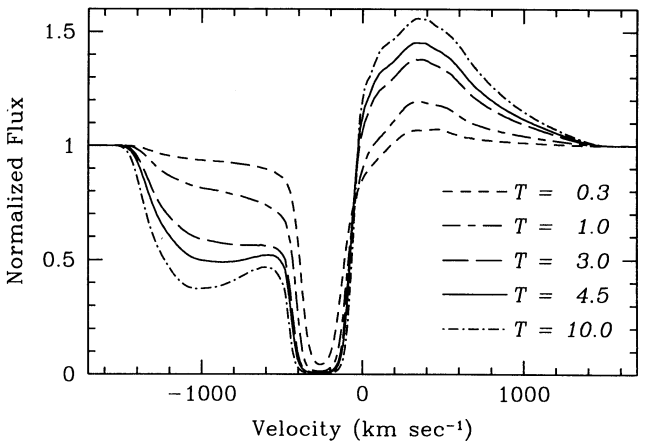

FIG. 11.—Comparison of profiles with different polar optical depths, T. Varying the optical depth is equivalent to changing the mass-loss rate, which increases the density throughout the wind. So, as the optical depth increases, the absorption and emission simultaneously increase at all wavelengths. Because the disk is much denser than the polar component, its absorption is stronger and saturates at smaller values of T than the polar component.

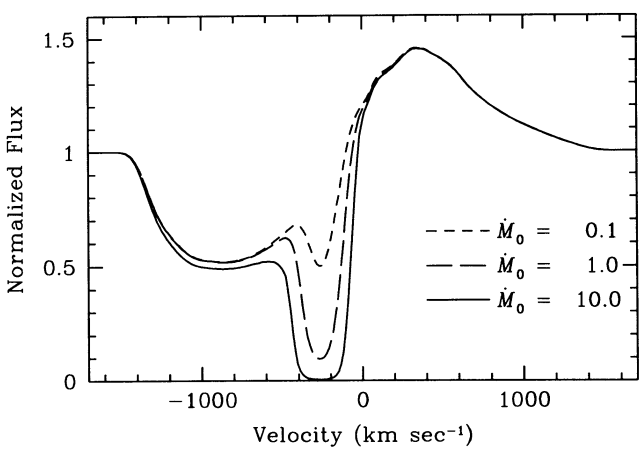

FIG. 10.—Comparison of profiles obtained by varying the ratio of the equatorial mass-loss rate to the polar mass-loss rate, $\dot{M}_0$. This changes the equatorial optical depth while maintaining a constant polar optical depth, and thus varies the strength of the low-velocity component. Note that the redshifted emission is hardly affected, because there is very little disk emission seen by an edge-on observer. The slight change in the absorption depth of the shelf is a numerical artifact.

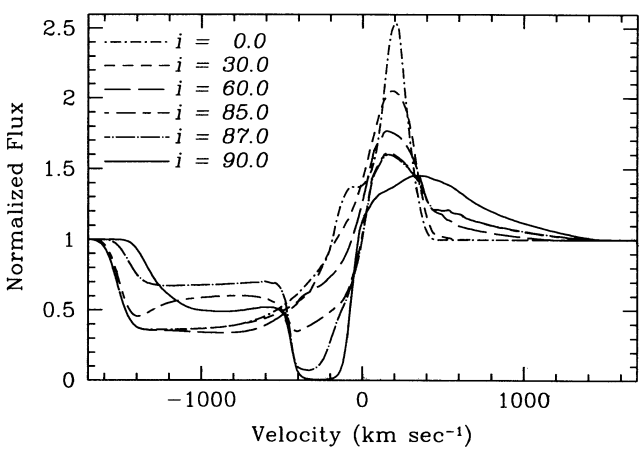

FIG. 12.—Comparison of profiles produced at different inclination angles, i. Note the extreme sensitivity of the strength of the low-velocity absorption component to the inclination angle; the disk absorption disappears for observers with $i < 85°$ and is saturated only for observers within the 3° opening angle of the disk ($i > 87°$).

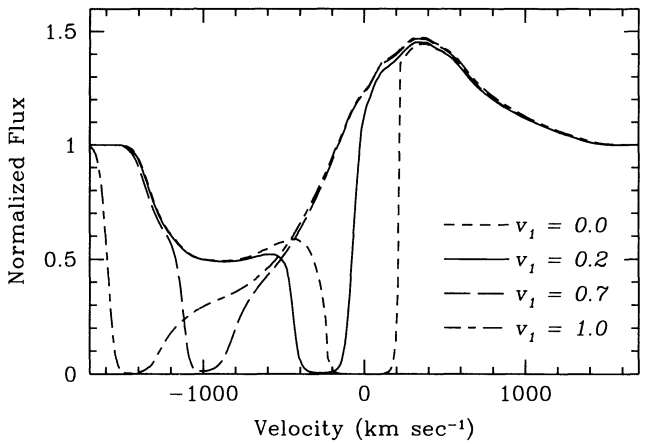

FIG. 13.—Comparison of profiles produced by disks with different terminal speeds ($v_1 \equiv v_\infty^{eq}/v_\infty^p$). Note that the low velocity absorption component shifts to higher velocity as v_1 is increased. The blue edge is determined by the terminal speed of the disk, v_∞^{eq}, and the red edge is determined by the velocity where the disk covers the entire star, $v_r^{eq}(r_c)$, which is $\propto v_\infty^{eq}$. As v_1 increases, both sides of the low-velocity absorption component shifts to higher velocity.

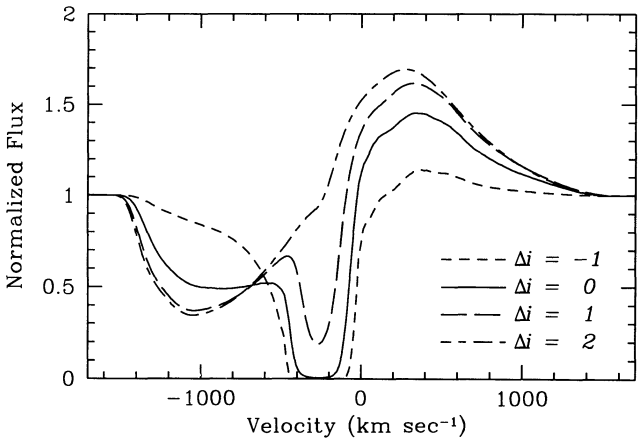

FIG. 15.—Comparison of profiles for different ionization states, Δi. Since the ionization fraction $q_i \propto (W/\rho)^{\Delta i}$, ions with $\Delta i = -1$ are destroyed in the polar component and enhanced in the dense disk. This produces a profile that has strong low-velocity absorption and weak high-velocity absorption. On the other hand, ions with $\Delta i = +2$ are enhanced in the polar component and destroyed in the disk, producing a profile with strong high-velocity absorption and almost no low-velocity absorption.

however, the profile does not remain black at the lowest velocities. This is a geometrical effect of the opening angle of the disk. To produce a black profile the entire star must be covered by the disk. For a given opening angle, it is only the material beyond a minimum radius, r_c, that covers the entire disk (see Fig. 8). This material corresponds to velocities from $v_c^{eq} \equiv v_r^{eq}(r_c)$ to v_∞^{eq}, so the low-velocity component can only be black in this velocity range.

Figure 14 shows how the profile changes with the disk opening angle, $\Delta\theta_d$. Observe the dramatic change in the high-velocity absorption component of the profile in going from a moderately thick disk to a very thin disk. Recall that the high-velocity absorption occurs *behind* the low-velocity disk absorption. This implies that there will be high-velocity absorption between $v = 0$ and $v = v_{edge}^p = v_r^p(r_c)$. As the disk becomes thinner, r_c becomes larger, so the high-velocity component absorbs out to higher velocities. Furthermore, the solid angle

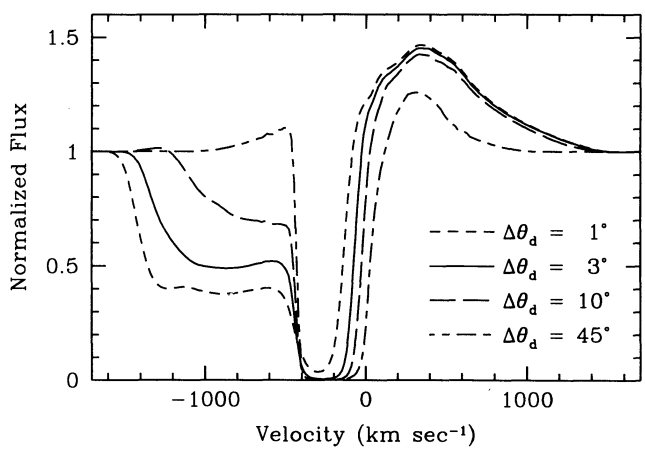

FIG. 14.—Comparison of profiles for disks with differing opening angles, $\Delta\theta_d$. For a disk viewed edge-on ($i = 90°$), a very thin disk (a few degrees or less) is required to obtain substantial absorption by the polar component at large velocities. Note that the depth of the high-velocity absorption is quite sensitive to the opening angle of the disk. In contrast, a thick disk exhibits blueshifted emission, because there is no high-velocity absorbing material (consider Fig. 8 with a thick disk).

of the star covered by the high-velocity component becomes larger as the solid angle of the disk becomes smaller. Therefore, the high-velocity component becomes blacker and absorbs to higher velocities as the disk gets thinner. Note that the absorption depth is quite sensitive to the disk opening angle. Finally, if the disk is thick enough, there is a very unusual feature—*blueshifted emission* out to the terminal speed of the polar component. This occurs because there is a no high-velocity absorption for a thick disk. One might think that the blueshifted emission could be the C IV blueshifted emission obtained using Howarth & Reid's (1993) continuum placement; however, *one cannot simultaneously obtain both a "shelf" and blueshifted emission.*

Figure 15 shows how the profile changes for lines with different ionization stages relative to the dominant ionization stage. If the line is two stages above the dominant ionization state, $\Delta i = +2$, the Sobolev optical depths are inversely proportional to the desnity, so the disk absorption component disppears. This is because the ion is almost completely destroyed by recombination in the dense disk. On the other hand, for lines that are one stage below the dominant state, $\Delta i = -1$, recombination in the disk increases the ionization fraction, so the disk absorption component becomes stronger.

5. A CASE STUDY: HD 93521

In the previous section, we have seen that the peculiar "shelf" feature of the C IV line profile of HD 93521 could be due to a wind that has an equatorial disk. Unfortunately, the individual components of the C IV doublet are separated by only 500 km s^{-1}, so the C IV doublet is strongly blended, and the low-velocity absorption in the blue-component overlaps the high-velocity absorption of the red component. This implies that the shelf feature, which is only seen in the C IV line, might be an artifact of the blending of the red and blue components.

To investigate this possibility, we used the spherically symmetric one-dimensional SEI method for doublets (Lamers et al., 1987). Ignoring any photospheric contribution, assuming no collisional (de)excitations, and using parameters that are similar to our fits for a two-dimensional geometry (discussed

below), we find that we can only fit the C IV line if the optical depth of the red component is about an order of magnitude larger than the blue component. This is physically impossible since the ratio of the optical depths between the red and blue components is given by the ratio of their oscillator strengths, which is about 1/2 (see Table 2). Thus the red component should instead have an optical depth about half that of the blue component.

Given that the shelf cannot be produced by line blending, we have chosen to employ our two-dimensional singlet code and ignore the effects of line blending. Our goal is to test the plausibility of a two-component geometry, not to include all of the detailed physics required to match the line profiles in detail. Instead, we are including the major effects that control the general shape of the profile. We feel that if we can reproduce the general shape of the profile, we will have demonstrated the plausibility of a two-component wind geometry.

5.1. *The Model Fits*

In this section, we simultaneously fit the C IV, Si IV, and N V profiles of the January 4 data set of HD 93521 to ascertain what we can quantitatively determine about the geometry and physical characteristics of the wind of HD 93521. First, it should be noted that our model does not include photospheric line absorption. Such absorption is symmetric about the line centers, so one can assess its significance by inspection of the redshifted absorption. Examining the redshifted absorption of the red component of each doublet shown in Figure 2, we see that, as expected for a spectral type of O 9.5, there is almost no N V, some C IV, and significant Si IV photospheric absorption. Second, we stress that our calculation is only valid for singlets. For this reason, when fitting a doublet, we present two separate curves—one for each component of the doublet. This is generally not a problem for the Si IV or N V lines because their individual components are well separated in velocity (i.e., $\Delta v > v_\infty^p$). However, blending is a problem for C IV, and unfortunately this ion is the best indicator of the geometry and flow characteristics.

To begin the fitting procedure, we note that the large $v \sin i$ and the nearly black low-velocity absorption implies that $i \sim 90°$ (see Fig. 12). Thus $V_{rot} \sim v \sin i = 400$ km s^{-1}. We must also choose a value for the Doppler width, v_D, to use for the line profile function. We use $v_D = 150$ km s^{-1}, which is about a tenth of the terminal speed and is within the range of turbulent velocities used by Groenewegen & Lamers (1989) in their study of O star winds.

TABLE 2

ATOMIC DATA—UV WIND LINES

Ion	λ (Å)[a]	f_{12}[b]	Ionization Potential[c] X^{i-1} (eV)	Ionization Potential[c] X^i (eV)
Si IV	1393.755	0.514	33.49	45.14
	1402.770	0.255		
C IV	1548.195	0.191	47.89	64.49
	1550.770	0.095		
N V	1238.821	0.157	77.47	97.89
	1242.804	0.078		

[a] Vacuum wavelength from Morton 1991.
[b] Oscillator strengths from Morton 1991.
[c] Ionization potential from Moore 1970. X^i is the ion listed in col. (1), and X^{i-1} is the next lower ionization stage (e.g., in the case of Si IV, X^{i-1} is Si III).

Our next step is to fit the C IV profile since it shows a shelf in the absorption, and the shelf feature is quite sensitive to the geometry of the disk. This fit determines the parameters describing the geometry of the two components, namely, the disk opening angle, $\Delta\theta_d$, the polar terminal speed of the wind, v_∞^p, the ratio of v_∞^{eq} to v_∞^p, v_1, and the ratio of equatorial to polar mass-loss rates, $\dot{M}_0$. Finally, when fitting the Si IV and N V profiles, the only free parameters that may be varied are those that indirectly govern the abundance and ionization fraction of the element; these parameters are T, Δi, and α. A description of the fit for each ion is presented hereafter.

5.1.1. C IV *Fits*

First, we must determine the terminal speeds of the two wind components. Referring to Figure 16, we estimate that the edge-velocity of the polar component is $v_{edge}^p \approx 1500$ km s^{-1}, and that the edge-velocity of the disk component is $v_{edge}^{eq} \approx 400$ km s^{-1}. The terminal speed of the disk is given $v_\infty^{eq} \approx v_{edge}^{eq} - v_D \approx 250$ km s^{-1} (for a discussion of how turbulence affects the edge velocity, see Lamers et al. 1987). Note that our assumed turbulent velocity is a significant fraction of v_∞^{eq} and is responsible for extending the deep absorption out from -250 to -400 km s^{-1}. To limit the total number of frequencies used in the line profile calculations (the frequency sampling is set by the minimum value of the Doppler width), we used a Doppler width in the disk that is the same as the polar Doppler width. However, it seems more reasonable to us that the turbulent velocity should scale with the flow velocity. This means that the Doppler width in the disk is probably too large. If the Dopple width in the disk were smaller, then the disk terminal speed would actually be closer to the edge-velocity of 400 km s^{-1}.

Finding the terminal speed of the polar component is more difficult, because the polar edge-velocity is determined by the polar flow velocity evaluated at the covering radius, r_c (see Fig. 8). Since this is dependent on the disk opening angle, $\Delta\theta_d$, finding the polar terminal speed is in fact an iterative process. Initially we assume $v_\infty^p \approx v_{edge}^p \approx = 1500$ km s^{-1}, which gives $v_1 \approx 1/6$. To actually fit the profile, we then vary T and $\Delta\theta_d$ until the redshifted emission and the depth and slope of the

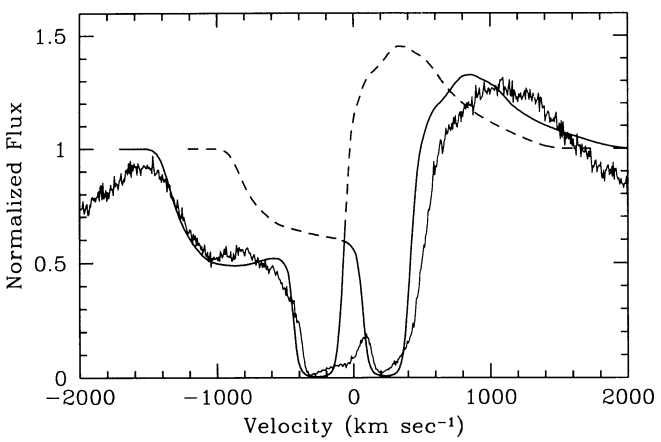

FIG. 16.—Two component fit to the C IV doublet of HD 93521. Since the theoretical model is for singlet lines, we present individual curves for each component of the doublet. The dashed portion of the fit indicates where we believe that the other line of the doublet dominates the shape of the profile. Note that when fitting the emission produced by the red component, we deliberately decreased the strength in an attempt to compensate for the increase in the red source function that occurs when the lines are blended.

high-velocity blueshifted absorption (i.e., the "shelf") is reasonably well matched by visual inspection. Note that T is constrained by the amount of redshifted emission and that $\Delta\theta_d$ is mostly determined by the depth of the high-velocity blueshifted absorption. Next we adjust the mass-loss ratio, M_0, to match the strength of the low-velocity absorption component. Finally, we correct the values of v_∞^p and v_1 to match the two absorption edges and repeat the fit.

We find that $v_\infty^p \approx 1500$ km s^{-1} and $\Delta\theta_d \approx 3°$ (see Table 3 for a complete list of parameters that describe the wind geometry). It is interesting that we require a very thin disk, because the WCD model predicts extremely thin disks of 1°–3° (Bjorkman & Cassinelli 1993; Owocki, Cranmer, & Blondin 1994). Our 3° disk opening angle yields a covering radius $r_c/R \approx 17$, and $v_r^p(r_c) \approx 1400$ km s^{-1}. Note that after correcting for the finite Doppler width, the edge-velocity is approximately the same as the polar terminal speed. Thus it is merely a coincidence that our initial guess, $v_{\rm edge}^p \approx v_\infty^p$, is the same as the results of our fit.

Now that we have discussed how we determine the geometry of the disk, we must also find the ionization distribution of C IV. To determine the ionization distribution, we attempted to fit the C IV line using several values of Δi and α. We find that the line is best fitted with $\Delta i = 0$ and $\alpha = 0$. As can be seen from equation (17), these values imply that the ionization fraction of C IV is approximately constant throughout the wind.

Figure 16 shows our best fit to the C IV data. The general shape of the two absorption components is well fitted; however, there is too little absorption in the model fit at the beginning of the shelf feature between -400 and -800 km s^{-1}. Since this is where the absorption of the red component begins, we expect that a proper handling of the blending of the doublet would increase the absorption at these velocities. Note that the blending would make the absorption steadily decrease in going blueward from low to high velocities, as seen in the data. The model fit also has too little emission at large positive velocities; this is intentional, because a singlet model underestimates the source function of the red component (see Olsen 1982). The last anomaly is the small emission bump near the rest-wavelength of the blue component. A zero-order approximation to accommodate doublet lines would be to multiply the absorption components of the singlet fits. One can see from Figure 16 that this would account for the bump as a result of the overlap of the doublet components.

5.1.2. Si IV *Fits*

As previously discussed, the fit to the C IV profile sets the geometrical parameters. Once the parameters describing the system's geometry and flow characteristics are fixed, the only remaining parameters that are allowed to vary for different lines are the polar optical depth and the parameters for the ionization fraction. We obtain the best qualitative fit to the Si IV line by using ionization parameters, $\Delta i = -1$ and $\alpha = 0$. From equations (15), (16), and (17), we see that $q_i \propto \rho/W$ and that the opacity $\kappa \propto \rho^2/W$. Thus the greatest opacity occurs in the high-density equatorial regions. This enhances the low-velocity absorption relative to the amount of polar emission (see Fig. 15).

Figure 17 shows the Si IV spectrum and our fit based on the geometry inferred from the C IV fit. We have attempted to match the small amount of redshifted emission, the deep low-velocity absorption component due to the disk, and the gradual slope of the high-velocity part of the profile. At first it would appear that our fit badly underestimates the high-velocity edge of the Si IV profile; however, an examination of the τ Sco *Copernicus* spectrum (Rogerson & Upson 1977) reveals that there are weak lines between 1386 and 1389 Å (-1700 to -1000 km s^{-1}), which when blended by the rotation speed of HD 93521 could cause the excess absorption. Similarly there are numerous lines in the τ Sco spectrum from 1409 to 1412 Å (3300–3900 km s^{-1}). Comparison of our fit to the data also shows that we do not have enough absorption near zero velocity, but Si IV is expected to have a strong photospheric line, which may also account for the redshifted absorption. Finally, the disk absorption component in our fit is too strong; matching the redshifted emission and the gradual slope of the profile at higher velocities requires an optical depth that causes too much absorption in the disk. This implies that our ionization law produces too much Si IV in the disk relative to the amount of Si IV in the polar regions.

5.1.3. N V *Fits*

Fitting the N V profile is much more problematic than either the C IV or Si IV profiles. An examination of Figure 18 reveals that N V has weaker disk absorption and stronger polar emission than C IV. Choosing $\Delta i = 2$ would completely destroy the disk absorption (see Fig. 15), so we adopt $\Delta i = 1$ and $\alpha = 0$ for our first attempt. These parameters imply that $q_i \propto W/\rho$ and $\kappa \propto W$, independent of the density. Examining Figure 18 we see that we fit the disk absorption for the blue component and the emission for the red component fairly well. Note that there is a C III line at 1247.4 Å near $+2100$ km s^{-1} which is destroy-

TABLE 3

MODEL GEOMETRY

Parameters	Values
i	90°
$\Delta\theta_d$	3°4
$R_*(R_\odot)$	8.0
T_*(K)	31,900
v_∞^p (km s^{-1})	1500
v_∞^{eq} (km s^{-1})	250
M_0	10.0

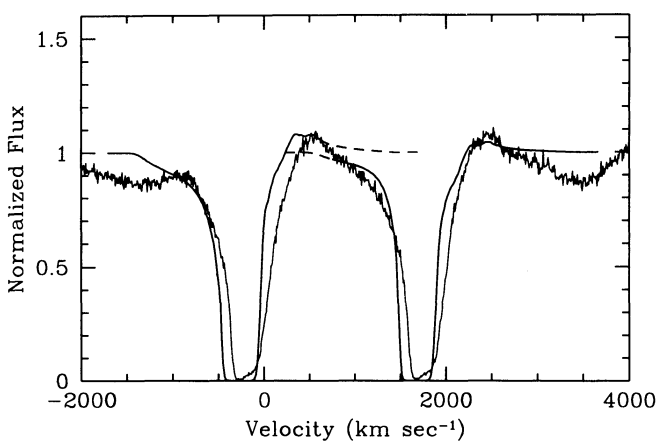

FIG. 17.—Two-component fit to the Si IV doublet of HD 93521. To fit the small amount of emission compared to the amount of absorption, we chose the ion state $\Delta i = -1$. This value is also required to match the slope of the high-velocity absorption component. Note that the "absorption dips" near -1500 and $+3500$ km s^{-1} may be due to weak photospheric line blends.

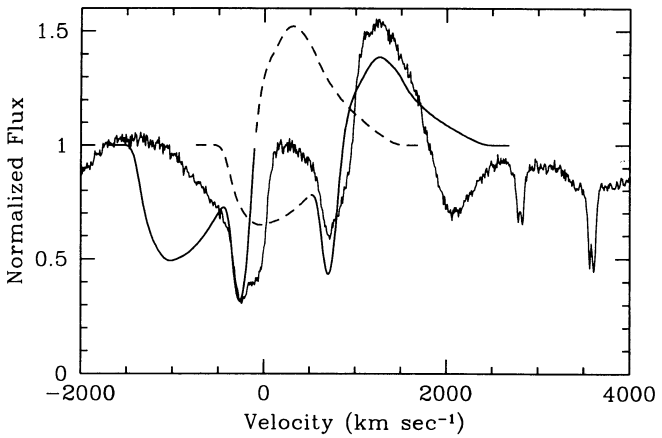

FIG. 18.—Two-component fit to the N v doublet emission of HD 93521. Shown here is our first attempt at fitting the N v doublet. We use $\Delta i = 1$ to enhance the emission relative to the equatorial absorption; however, there is clearly an unacceptable amount of high-velocity absorption. Also the disk absorption strength of the red component is too large, but there is emission from the blue component at these velocities that will tend to reduce the amount of absorption.

ing part of the redshifted emission. Although the absorption for the red component in the disk is too large, this is probably a result of neglecting the line blending. There is, however, one effect we cannot account for: the deep absorption and sharp edge at high velocity. This implies that our fit has too much absorption at high velocity in the polar component.

We can destroy the ion at large radii by setting α to a large positive number. Models of the ionization equilibrium of O star winds (Drew 1989) indicate that for a spectral type of O 9.5 V, the ionization fraction of N v is approximately a power law with radius that can be fitted by choosing $\Delta i = 0$ and $\alpha = 7$ (however, these models do not include photoionization by X-rays, which substantially changes the ionization equilibrium). As seen in Figure 19, we can crudely fit the disk absorption depth and the high-velocity slope of the profile with $\Delta i = 0$ and $\alpha = 7$, but we have lost all of the emission. This is because the steep power law in the ionization fraction places all the emitting material near the star ($\kappa \propto \rho r^{-\alpha}$), which greatly reduces the effective emitting volume.

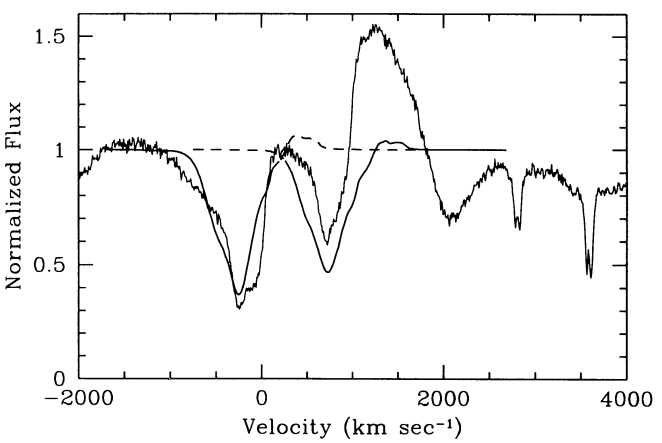

FIG. 19.—Two-component fit to the high-velocity absorption component of the N v doublet. Shown here is our second attempt at fitting the N v line. To reduce the amount of absorption at large radii, we use a power law, $q \sim r^{-7}$, for the ionization fraction. This fits the high-velocity absorption much better, but now there is hardly any emission, because the material has been placed so close to the star that the emitting volume is much too small.

Our first two attempts to fit the N v profile have matched two extremes of the profile; one fits the emission and the other fits the absorption. For this reason, we attempted a composite fit that assumed different ionization parameters for the disk and polar components; however, we were unable to find a set of parameters that would simultaneously fit both the observed absorption and emission. The fundamental problem for simultaneously matching the polar absorption and emission is that the emission equivalent width is larger that the absorption equivalent width. Since the polar component is almost spherically symmetric, a scattering line, which conserves photons, will never produce more emission than absorption. Either collision excitation is important for N v and unimportant for C IV (this seems unlikely since their wavelengths imply that the excitation energies are not very different), or the polar component cannot be spherically symmetric. In the WCD model of Bjorkman & Cassinelli (1993), the density of the polar component is almost constant with latitude, *except near the disk*, where there is an increase in density by about a factor of 10. If the ionization fraction of N v is more sensitive to density than the C IV ionization fraction, then the higher recombination rates, just above and below the disk, might destroy N v relative to C IV. This would greatly reduce the high-velocity N v absorption and might serve to explain how the polar emission equivalent width can be larger than the absorption equivalent width for N v but not for C IV.

Clearly, to study this possibility requires identifying mechanisms that reduce the ionization fraction at low latitudes. The ionization balance is fundamentally governed by recombination versus photoionization by the star or by X-rays produced in the wind. As mentioned above, latitudinal density gradients will affect the recombination rates, but a different way to cause latitudinal ionization gradients is if the photoionization flux has a latitudinal gradient. Massa (1992) has already demonstrated that HD 93521 exhibits gravity darkening, so the photosphere is cooler at the equator than at the pole. This results in fewer ionizing photons in the equatorial region, which will lower the ionization state near the disk. Since N v has a higher ionization potential than C IV it will be more severely affected than C IV. Thus gravity darkening could also play a role in explaining the anomalously large N v emission to absorption ratio.

5.2. *Derived Quantities*

In this section, we derive values for the column density, N_i, and the product $\dot{M}_p q_{1/2,i}$ for each ion. Table 4 summarizes the optical depth, T, and ionization parameters (Δi and α) that we used to fit the line profile of each ion. Table 4 also lists the associated normalization constants, $q_{0,i}$, given by equation (18), and $I(\Delta i, \alpha)$, given by equation (22). Using the optical depths, we calculate the column density from equation (20). (See Table 2 for wavelengths and oscillator strengths and Table 3 for the polar terminal speed.) The results are listed in the next to last column of Table 4.

Given the column densities, we compute $\dot{M}_p q_{1/2,i}$ for each ion from equation (23), which requires the abundance, A_E, for each element and the mass fraction of hydrogen, X. We use the solar abundances of Grevesse & Anders (1989): log(C/H) = −8.56, log (Si/H) = −7.55, and log (N/H) = −8.05, which gives $X \approx 0.7$. Using the values listed in Table 4 for $q_{0,i}$ and $I(\Delta i,\alpha)$ along with these abundances, we tabulate log $\dot{M}_p q_{1/2,i}$ for each ion in the last column of Table 4. Note that if instead we were to use the B star abundances of Gies &

TABLE 4

LINE FITS

Ion	T	Δi	α	$q_{0,i}$	$I(\Delta i, \alpha)$	N_i (10^{15} cm^{-2})	log $\dot{M}_p q_{1/2,i}$ ($M_\odot$ yr^{-1})
C IV	4.7	0	0	1.0	4.7	9.0	−9.7
Si IV	3.3	−1	0	7.5	238	2.6	−10.1
N V[a]	2.0	1	0	0.13	0.29	5.8	−9.0
N V[b]	10.4	0	7	0.007	2.3	30.3	−10.5

[a] Corresponds to the N V line fit to the emission.
[b] Corresponds to the N V line fit to the absorption.

Lambert (1992), $\dot{M}_p q_{1/2,i}$ would increase by about a factor of 2 for C IV and N V but would remain about the same for Si IV.

Finally, we also determine the ratios of the ionization fractions. Given parameters from Table 4 and the solar abundances, we use equation (24) to evaluated the ratio of ionization fractions at $v/v_\infty = 1/2$, which gives the following ratios:

$$\frac{q_{1/2,\mathrm{Si\,IV}}}{q_{1/2,\mathrm{C\,IV}}} = 0.5 ,$$

$$\frac{q_{1/2,\mathrm{N\,V}}}{q_{1/2,\mathrm{C\,IV}}} = 4.5 \quad \text{(N V emission)} ,$$

$$\frac{q_{1/2,\mathrm{N\,V}}}{q_{1/2,\mathrm{C\,IV}}} = 0.2 \quad \text{(N V absorption)} .$$

Note that the first occurrence of N V corresponds to the fit to the emission, shown in Figure 18, and the second is for the fit to the absorption, shown in Figure 19.

To check if our column densities and mass-loss rates are reasonable, we compare our values to the results of two separate studies, one theoretical and one observational. First, we compare our results to the theoretical ionization equilibrium models of steady-state, spherically symmetric wind flows calculated by Drew (1989). We consider only the polar region of our model, since it is almost spherically symmetric (due to the thinness of the disk). Figures 5, 6, and 8 of Drew (1989) show the ionization fraction for ions of carbon, nitrogen, and silicon, respectively, versus stellar temperature. These models indicate that we should expect C IV, N IV, an Si V to be the dominant ions at temperatures of about 31,900 K (i.e., an O 9.5 V star). This implies $\Delta i = 0$ for C IV, $\Delta i = -1$ for Si IV, and $\Delta i = 1$ for N V, which are the same parameters chosen for our fits (see Table 4). However, this interpretation has two problems: (1) We expect log $\dot{M} \approx 1.69$ log $(L_*/L_\odot) - 15.4 \approx -7.2$ (Howarth & Prinja 1989). If C IV were dominant, then $q_{\mathrm{CIV}} \sim 1$, which would imply that our results in Table 4 should give log $\dot{M}_p q_{1/2} \sim$ log $\dot{M}_p \sim -9.7$, which is much smaller than the expected mass-loss rate. Thus C IV cannot be the dominant ionization state. (2) A value of $\Delta i = 1$ for the N V profile does not fit the high-velocity absorption (see Fig. 18); the model predicts too much absorption.

We also compare our results to the observational study of Howarth & Prinja (1989) who included HD 93521 in their sample of 203 O stars. They determined column densities, $N_i/10^{15} = 6.74$, 0.0550, and 1.08 cm^{-2} for C IV, Si IV, and N V, respectively (see Table 6 of their paper). These values agree with ours to order of magnitude for C IV and N V; however, our column density for Si IV is about two orders of magnitude larger. The discrepancy can be attributed to two effects: (1) As discussed in § 5.1.2., we ignore the strong photospheric contribution of the absorption for Si IV, thus our fit overestimates the optical depth, T, which is proportional to the column density. (2) Howarth & Prinja use a smaller terminal speed, $v_\infty \sim 1000$ km s^{-1}. This lowers their column densities relative to ours as can be seen by equation (20).

Howarth & Prinja also compute log $\dot{M} q_{1/2,i}$ and log $(q_{1/2,i} A_E/A_\odot)$ for each line. They find log $\dot{M} q_{1/2,i} = -9.7$, -10.8, and -9.9 for C IV (a lower limit), Si IV (an upper limit), and N V, respectively (see Table 10 of their paper). Comparison with Table 4 shows that our values for $\dot{M}_p q_{1/2,i}$ are in fairly good agreement with those of Howarth & Prinja.

We observe the following: (1) Our $\dot{M}_p q_{1/2}$ for Si IV is nearly an order of magnitude larger than that of Howarth & Prinja (1989), for reasons previously discussed. (2) Howarth & Prinja derive a value of $\dot{M} q_{1/2}$ for N V which is between those derived for our two extreme fits. (3) Howarth & Prinja (1989) find log $\dot{M} = -7.2$ and log $(q_{1/2} A_E/A_\odot) > -2.5$ for C IV, which agrees with our $\dot{M}_p q_{1/2}$ and disagrees with Drew's (1989) study that indicates that C IV should be the dominant ion. Although we found $\Delta i = 0$, which supports Drew's conclusion that $q \approx$ constant, we infer that C IV cannot be the dominant ion, because $q_{1/2} \ll 1$. In fact, Drew addresses this problem when she compares the results of her theoretical calculations to the sample of Howarth & Prinja (see Fig. 23 of her paper). Her model overestimates $\dot{M} q_{1/2,i}$ by one to three orders of magnitude (the discrepancy is worse for the cooler O stars). Drew suggests that the discrepancy is due to the photoionizing effects of X-rays produced by shocks, which are not included in her model. We believe that the most likely explanation is that these X-rays tend to make C V the dominant ion and they must also have a distribution such that $q \approx$ constant for C IV.

6. CONCLUSIONS

Both *IUE* and *HST* observations of HD 93521 show a peculiar C IV P Cygni line profile that has two absorption edges connected by a "shelf." Comparison of two *HST* observations (taken on different dates) indicates the presence of variability from the high-velocity edge down to zero velocity (and below). These LSA data appear to show blue edge variability in the low-velocity absorption component; however, the low-velocity edge variability is probably an artifact of two NACs that were clearly resolved by the SSA data. In addition to the presence of multiple NACs, there is also a low velocity feature, which could be due to a discrete emission "blob" in the wind.

Motivated by the two absorption components seen in C IV, we investigated the effects of a two-component wind geometry on the shape of the P Cygni profiles of the UV resonance lines. The general shape of the profile may be qualitatively understood as the composition of two separate P Cygni profiles: one for the low-speed disk and a second for the high-speed wind in the polar regions. For thin disks, the net result if that the profile appears to be a normal P Cygni profile with either a

low-velocity absorption component (when the disk is viewed edge-on) or a narrow emission spike (when the disk is viewed pole-on). For edge-on thick disks, there is no high-velocity absorption, so absorption occurs only in the low-velocity disk. In this case, the profile exhibits only the polar emission with a narrow low-velocity absorption component from the disk, so this profile has blueshifted emission between the terminal speed of the disk and the terminal speed of the polar component.

To produce a line profile with a shelf, as observed in HD 93521, requires a thin disk, and the inclination angle of the star must place the observer within the opening angle of the disk. For HD 93521 the disk must have an opening angle of about 3°, so the inclination angle must be larger than about 87°. Note that the probability of observing a star within such a small range of inclination angles is only about 6%. From our fits to the C IV line profile, we find that the terminal speed of the polar component is 1500 km s^{-1}, and the terminal speed in the disk is between 250 and 400 km s^{-1}. The best fit to the profile is obtained if the ionization fraction, q, of C IV is a constant independent of position. The polar optical depth gives the column density of C IV and determines the product $\dot{M}q_{1/2} = 2 \times 10^{-10}\ M_{\odot}\ \mathrm{yr}^{-1}$. Because this is much smaller than the expected mass-loss rate, the ionization fraction of C IV must be much less than one, which implies that C IV is not the dominant ionization state, even though it has constant ionization fraction. From the strength of the low-velocity absorption, we find that the mass flux in the disk is about 10 times larger than the polar mass flux, which implies a density ratio, $\rho_{eq}/\rho_p = 60$. Note that the geometry for the disk is similar to that predicted by the wind-compressed disk model of Bjorkman & Cassinelli (1993).

Using the geometry obtained from fitting the C IV profile, we also fit the Si IV and N V profiles. Because the Si IV emission is weak relative to the amount of absorption in the disk, the ionization fraction of Si IV must increase with increasing density. Thus our best fit is obtained when we assume that Si IV is one stage below the dominant ionization state, which would be Si V. On the other hand, the N V emission is strong relative to the amount of disk absorption, so our best fit to the amount of emission occurs when N V is one stage above the dominant state. However, using the same disk geometry as for C IV, we are unable to simultaneously match the absorption and emission strengths of N V; the emission is anomalously strong in comparison to the amount of high-velocity absorption. We view this as evidence for a latitudinal ionization gradient of N V in the polar part of the flow. This latitudinal ionization gradient could be caused by either a latitudinal density gradient or perhaps by the effect of gravity darkening on the photoionizing flux.

There has been considerable debate whether HD 93521 is a Population I or II star, because the luminosity is required for distance estimates. The distance is important for studies of the structure of the ISM, such as Spitzer & Fitzpatrick (1993), which may place important constraints on the ionization source for the ISM. Our estimate of the terminal speed of HD 93521 bears on this question, because the terminal speed can be used to estimate the escape speed, and, when combined with the surface gravity, $\log g$, yields an estimate of the stellar radius (see Howarth & Reid 1993). Our terminal speed of 1500 km s^{-1} is somewhat lower than Howarth & Reid's value of 2000 km s^{-1}, so in principle it would decrease the estimated distance to HD 93521. However, the change in distance is much less than the errors quoted in Howarth & Reid, and our estimate of the escape speed is still well within the acceptable range of Howarth & Reid's Population I solutions.

In summary, we fit P Cygni line profiles using an axisymmetric two-component wind geometry, and we have seen that one may be able to obtain important constraints, such as the terminal speed of the wind, inclination angle of the star, and opening angle of the disk. In fitting the profiles, the amount of emission is a useful constraint on the optical depth of the polar component. However, since most of the resonance lines are actually doublets, the emission strength of the red component of the line depends on the nonlocal coupling between the source functions of the red and blue components. For this reason, if one wishes to make more accurate estimates of the wind geometry than presented in this paper, it will be essential to account for this nonlocal coupling. Another issue that is critical to the accurate calculation of line profiles is the ionization balance as a function of position in the wind. In this paper we have seen that there may be important differences between high ionization stages like N V and lower stages like C IV. In particular, there is the suggestion that the ionization fraction depends on latitude via the density. This offers the possibility that one might be able to obtain information about the latitudinal density structure of the wind *if* one is able to adequately model the ionization fraction as a function of position for different lines.

We would like to credit Derck Massa for suggesting this problem, and we thank Henny Lamers, Joe MacFarlane, and Alex Fullerton for useful discussions. Ken Sembach provided software (IMNORM, version 5.0), which was used for the analysis of GHRS data. We especially thank Ken for modifying the software to suit our particular needs. This work was funded by STScI grant AR-3749-02-91A and NSF grant AST-9115375. T. M. T. acknowledges support from the NASA Graduate Student Researchers Program through grant NGT 51003.

REFERENCES

Abbott, D. C. 1978, ApJ, 225, 893
Bisiacchi, G. F., Carracso, C., Costero, R., & Firmani, C. 1978, Rev. Mexicana Astron. Af., 2, 309
Bjorkman, J. E., & Cassinelli, J. P. 1993, ApJ, 409, 429
Bjorkman, J. E., Sembach, K. R., & Watson, A. 1994, in preparation
Burrows, C. J., Holtzman, J. A., Faber, S. A., Bely, P. Y., Hasan, H., Lynds, C. R., & Schroeder, D. 1991, ApJ, 369, L21
Castor, J. I. 1970, MNRAS, 149, 111
Castor, J. I., & Lamers, H. J. G. L. M. 1979, ApJS, 39, 481
Conti, P. S., & Ebbets, D. 1977, ApJ, 213, 438
Drew, J. E. 1989, ApJS, 71, 267
Ebbets, D. C. 1992, Final Report of the Science Verification Program for the Goddard High Resolution Spectrograph for the Hubble Space Telescope, prepared for NASA/Goddard Space Flight Center by Ball Aerospace Systems Group
Ebbets, D. C., & Savage, B. D. 1982, ApJ, 262, 234
Fullerton, A. W. 1994, in IAU Symp. 162, Pulsation, Rotation, and Mass-Loss in Early-Type Stars, ed. L. A. Balona & H. F. Henrichs (Dordrecht: Kluwer), in press
Gies, D. R., & Lambert, D. L. 1992, ApJ, 387, 673
Gilliland, R. L., & Hulbert, S. J. 1993, GHRS Instrument Science Report 055, Space Instruments Branch, (Baltimore: Space Telescope Science Institute)
Gilliland, R. L., Morris, S. L., Weymann, R. J., Ebbets, D. C., & Lindler, D. L. 1992, PASP, 104, 367

Grevesse, N., & Anders, E. 1989, in Cosmic Abundances of Matter, ed. C. J. Waddington (New York: AIP), 1
Groenewegen, M. A. T., & Lamers, H. J. G. L. M. 1989, A&AS, 79, 359
Guetter, H. H. 1974, PASP, 86, 795
Hamann, W.-R. 1980, A&A, 84, 342
———. 1981, A&A, 93, 353
Hobbs, L. M., Morgan, W. W., Albert, C. E., & Lockman, F. J. 1982, ApJ, 263, 690
Howarth, I. D., & Prinja, R. K. 1989, ApJS, 69, 527
Howarth, I. D., & Reid, A. H. N. 1993, A&A, submitted
Irvine, N. J. 1989, ApJ, 337, L33
Kurucz, R. L. 1974, ApJ, 188, L21
Lamers, H. J. G. L. M., Cerruti-Sola, M., & Perinotto, M. 1987, ApJ, 314, 726
Lamers, H. J. G. L. M., & Morton, D. C. 1976, ApJS, 32, 715
Lindler, D. 1993, BAAS, 25, 831
Massa, D. 1992, in Nonisotropic and Variable Outflows from Stars, ed. L. Drissen, C. Leitherer, & A. Nota (ASP Conf. Series 22), 84
Mazzali, P. A., Berger, C. A., & Henrichs, H. F. 1990, in ESO Conf. Proc. 36, Rapid Variability of OB-Stars: Nature and Diagnostic Values, ed. D. Baade & P. J. Grosbøl (Garching bei München: ESO), 223
Mihalas, D., Kunasz, P. B., & Hummer, D. G. 1975, ApJ, 202, 465
Moore, C. E. 1970, Ionization Potentials and Ionization Limits Derived from the Analysis of Optical Spectra, Report NSRDS-NBS 34, U.S. Department of Commerce, Washington, D.C.
Morton, D. C. 1991, ApJS, 77, 119
Olson, G. L. 1982, ApJ, 255, 267
Owocki, S. P., Cranmer, S. R., & Blondin, J. M., 1994, ApJ, 424, 887
Prinja, R. K. 1988, MNRAS, 231, 21P
Prinja, R. K., & Howarth, I. D. 1986, ApJS, 61, 357
———. 1988, MNRAS, 233, 123
Ramella, M., Morossi, C., & Santin, P. 1980, A&A 90, 146
Rogerson, J. B., & Upson, W. L. II. 1977, ApJS, 35, 37
Rybicki, G. B., & Hummer, D. G. 1978, ApJ, 219, 654
Savage, B. D. 1991, in The First Year of HST Observations, ed. A. L. Kinney & J. C. Blades (Baltimore: Space Telescope Science Institute), 33
Sofia, U. J., Savage, B. D., & Cardelli, J. A. 1993, ApJ, 413, 251
Spitzer, L., & Fitzpatrick, E. L. 1992, ApJ, 391, L41
———. 1993, ApJ, 409, 299
Swings, J. P., & Vreux, J. M. 1976, A&A, 52, 161